From GDE half-cell screening to single-cell validation: impact of ionomer chemistry and I/C ratio on PEMFC catalyst-layer structure and performance

Fuel 428 (2027) 140521

Contents lists available at ScienceDirect

Fuel

journal homepage: www.elsevier.com/locate/fuel

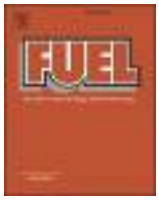

Full Length Article

From GDE half-cell screening to single-cell validation: impact of ionomer chemistry and I/C ratio on PEMFC catalyst-layer structure and performance

Giovanni Marco Carrabba, Maria Chiara Massaro, Erik Piatti, Enrico Sartoretti, Alessandro Hugo Antonio Monteverde *

Politecnico di Torino, Department of Applied Science and Technology, Corso Duca degli Abruzzi, 24, 10129 Torino, Italy

ARTICLE INFO

Keywords:
Proton exchange membrane fuel cell (PEMFC)
Ionomer-catalyst interactions
Gas diffusion electrode (GDE)
Ionomer-to-carbon ratio (I/C)
Iononer distribution
Half-cell and single-cell validation

ABSTRACT

Understanding how ionomer chemistry governs catalyst-layer architecture is critical for the rational design of proton exchange membrane fuel cells (PEMFCs). In this work, we establish a multi-scale experimental framework that integrates gas diffusion electrode (GDE) half-cell screening, advanced structural characterization, and single-cell validation to directly correlate ionomer chemistry, catalyst-layer microstructure, and electrochemical performance. Using Nafion® and two short-side-chain Aquivion® ionomers (D79 and D98) as model systems, GDE screening identifies an optimal ionomer-to-carbon ratio (I/C = 0.6) and captures intrinsic activity trends that are subsequently validated under single-cell operation. Lower equivalent weight ionomers enhance proton transport by forming more connected ionomer networks, but also promote denser catalyst layers that reduce pore accessibility and lead to mass-transport losses at high current density. In contrast, more open architectures improve oxygen transport and water management, enabling superior full-cell performance despite lower intrinsic proton conductivity. These results establish a general design principle for PEMFC electrodes: optimal performance arises from balancing ionomer connectivity and pore accessibility, rather than maximizing ionomer conductivity alone. More broadly, this work demonstrates that GDE half-cell testing is a predictive and resource-efficient platform for catalyst-layer optimization, capable of decoupling proton transport from structural effects and linking electrochemical descriptors to microstructural features, while also highlighting its limitations under realistic PEMFC operating conditions.

1. Introduction

The catalyst layer (CL) represents the core functional component of proton exchange membrane fuel cells (PEMFCs), as it hosts the electrochemical reactions and governs the overall efficiency of energy conversion. Its performance is critically determined by the effective formation and stability of the triple-phase boundary (TPB), where gaseous reactants, electronic conductors, and proton-conducting ionomer domains coexist and interact [1,2]. Non-uniform ionomer coverage, heterogeneous Pt–ionomer interfaces, and locally isolated catalytic domains can significantly reduce the effective TPB and limit catalyst utilization [3–5]. Consequently, engineering a well-connected, percolated triple-phase interface is essential to maximize proton accessibility, oxygen transport, and electrochemical activity within the CL.

Within this framework, the ionomer plays a central role in defining the structural and functional properties of the CL, as it governs the balance between proton conduction, gas transport, and catalyst accessibility. Among the parameters controlling ionomer distribution, the ionomer-to-carbon (I/C) ratio is particularly critical, as it directly influences the extension and connectivity of the TPB [1,6,7].

High I/C ratios (≥ 0.8) promote the formation of a continuous ionomer network, enhancing proton conduction and charge transport, particularly at low and medium current densities [7,8]. However, excess ionomer can block the porous structure of the carbon support, hindering oxygen diffusion and leading to significant mass-transport limitations at high current densities [1,7]. Conversely, low I/C ratios (≤ 0.4) preserve CL porosity and facilitates gas transport, but limits proton conduction, since the ionomer network becomes discontinuous and insufficient to guarantee efficient access to catalytic sites [7,8]. The optimal I/C ratio therefore represents a trade-off between proton conduction and oxygen diffusion.

In PEMFCs applications, perfluorosulfonic acid (PFSA) ionomers remain the industrial benchmark, with Nafion® as a widely used long-

* Corresponding author.
E-mail address: alessandro.monteverdevidela@polito.it (A.H.A. Monteverde).

https://doi.org/10.1016/j.fuel.2026.140521
Received 4 February 2026; Received in revised form 26 May 2026; Accepted 27 June 2026
Available online 2 July 2026

Nomenclature

Acronyms

AC	Alternating Current
AFM	Atomic Force Microscopy
BJH	Barrett–Joyner–Halenda method
CL	Catalyst Layer
CV	Cyclic Voltammetry
DOE	Department of Energy (USA)
ECSA	Electrochemical Surface Area
EIS	Electrochemical Impedance Spectroscopy
EW	Equivalent Weight
FESEM	Field Emission Scanning Electron Microscopy
GDE	Gas Diffusion Electrode
GDL	Gas Diffusion Layer
HR	High Resolution
IEC	Ion Exchange Capacity
I/C	Ionomer-to-Carbon Ratio
IR	Infrared
LSC	Long Side Chain
LSV	Linear Sweep Voltammetry
MEA	Membrane Electrode Assembly
MPL	Microporous Layer
OCV	Open Circuit Voltage
PEMFC	Proton Exchange Membrane Fuel Cell
PFSA	Perfluorosulfonic Acid
PTFE	Polytetrafluoroethylene
R_0	Ohmic Resistance
R_{ct}	Charge Transfer Resistance
RDE	Rotating Disk Electrode
RH	Relative Humidity
RHE	Reversible Hydrogen Electrode
SA	Surface Area
SEM	Scanning Electron Microscopy
SSC	Short Side Chain
TPB	Triple Phase Boundary
XPS	X-ray Photoelectron Spectroscopy

side-chain (LSC) polymer [9]. Nafion® features a hydrophobic perfluorinated backbone and long pendant sulfonic acid-terminated side chains, which form the hydrophilic domains responsible for proton conduction [7,10]. Conversely, short-side-chain (SSC) PFSA ionomers such as Aquivion® feature a much shorter side chain, higher sulfonic acid site density, and a reduced number of vulnerable ether and tertiary-carbon linkages [11–15].

Among SSC ionomers, several grades exist that differ in their equivalent weight (EW)—a parameter reflecting the density of acid groups along the polymer chain [13–17]. Low-EW ionomers, such as Aquivion® D79, therefore exhibit superior proton conductivity and water uptake compared to higher-EW analogues and to Nafion® [5,11–20]. While enhanced hydration is advantageous under dry or high-temperature operation [21,22], excessive water retention can increase oxygen transport resistance and flooding under high-RH conditions or not optimized I/C ratios [4,7,23].

LSC and SSC ionomers also differ in crystallinity and glass transition temperature (T_g) [13,15]. Shorter and more closely spaced side chains in SSC ionomers promote the formation of compact crystalline domains, resulting in higher crystallinity and T_g than LSC analogues [13,15], thus reducing swelling and enhancing dimensional stability, mechanical robustness and interfacial durability [17,24,25]. However, the higher rigidity limits flexibility, increasing the risk of microcrack formation during hydration–dehydration cycles, particularly in the ultra-thin ionomer films of the CL [4,5]. In contrast, Nafion®, with its longer and flexible side chains, is mechanically more compliant and better accommodates hydration-induced stresses, but it is more susceptible to swelling, morphological coarsening, and long-term delamination from the catalyst surface [10,17].

The key physicochemical parameters of Nafion® and Aquivion® are summarized in Table 1.

Beyond this quantitative trade-off, the optimal I/C ratio strongly depends on the specific chemistry and interfacial interactions of the ionomer with Pt and carbon surfaces, which ultimately determine its

Table 1
Comparative characteristics of Nafion® and Aquivion® ionomers.

Property	Nafion®	Aquivion®
Chemical structure[a]	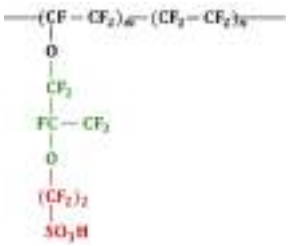	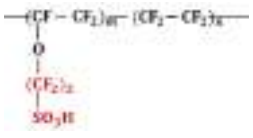
Equivalent Weight [14,15]	~1100 g mol^{-1}	~720 – 980 g mol^{-1}
Ion Exchange Capacity [13,20]	~0.91 m_{eq} g^{-1}	1.26 – 1.40 m_{eq} g^{-1}
Water Uptake[b] (80 °C, 90% RH) [11]	≈ 6	≈ 6.5–8
Glass Transition Temperature [13,15]	110 – 115 °C	120 – 140 °C
Proton conductivity (100% RH, 80 °C) [26,27 16,18]	0.08 – 0.13 S cm^{-1}	>0.23 S cm^{-1}
Proton conductivity (30% RH, 80 °C) [15]	~0.01 S cm^{-1}	0.02 – 0.03 S cm^{-1}
Proton conductivity at > 90 °C [17,20]	Conductivity collapse > 100 °C (without pressurization)	~0.1 S cm^{-1} (120 °C, 100% RH)
Hydrogen crossover [15]	~1.6 mA cm^{-2}	~1.2 mA cm^{-2}
Strengths	Flexible, durable, benchmark performance	Balanced conductivity and stability
Weaknesses	Lower conductivity at low RH, thicker films	More rigid than Nafion®, flooding risk if I/C not optimized

[a] In SSC ionomers, the equivalent weight is determined by the ratio of non-substituted tetrafluoroethylene units (n) to side-chain-bearing units (m), which dictates the frequency of acid groups along the polymer backbone [11–15].

[b] Water uptake is defined as the number of water molecules absorbed per sulfonic acid group of the ionomer thin films at 90%RH [11].

nanoscale distribution and functional effectiveness within the CL. Optimizing the I/C ratio for each ionomer is essential to fully exploit the specific advantages related to their physicochemical nature.

The literature has shown that Aquivion® ionomers need lower I/C ratios than Nafion® for optimal performance [4,5], as excessive SSC ionomer loading may clog mesopores, increasing transport resistance and flooding [4,7,23]. When properly optimized, Aquivion®-based CLs consistently deliver higher electrochemical surface area (ECSA), enhanced Pt utilization, and superior performance—particularly under low-RH and high-temperature conditions [17,20,25,28]. In contrast, Nafion®-based CLs generally need higher ionomer contents to preserve adequate proton conductivity under moderate humidity, though this often comes at the expense of increased oxygen-transport resistance [7,23].

Therefore, achieving optimal CL performance requires balancing ionomer content, microstructure, and operating conditions—where SSC ionomers excel under low-humidity, high-temperature environments, while Nafion® remains well-suited to moderate-humidity and standard automotive applications [3,10,24].

Despite this extensive understanding of ionomer chemistry and structure–property relationships, isolating the specific effect of the ionomer on CL performance within full MEAs remains challenging. In full-cell testing, multiple overlapping phenomena—including water management, membrane hydration, and crossover—can obscure the intrinsic impact of ionomer type, I/C ratio, and distribution on TPB formation and catalyst utilization.

To address this limitation, the gas diffusion electrode (GDE) half-cell has emerged as a promising methodology. In this setup, the CL is deposited on a porous gas diffusion layer (GDL) and simultaneously exposed to a liquid electrolyte on the CL side and a controlled flow of reactant gas on the GDL side [29–34]. This dual exposure recreates the TPB under semi-realistic conditions, allowing simultaneous supply of protons, electrons, and reactants. Compared to rotating disk electrode (RDE) experiments, the GDE bypasses oxygen solubility limitations, enabling current densities up to 1–2 A cm^{-2} and evaluation of both kinetic and transport-relevant regimes [29–34]. The platform also allows testing of electrodes with realistic catalyst loadings (0.10–0.20 mg_{Pt} cm^{-2}) and micrometric thicknesses, capturing effects of ionomer distribution and Pt accessibility that are critical in practical devices [29–34]. Its main limitation lies in the inability to fully reproduce all aspects of real fuel cell operation. In particular, it lacks a proton exchange membrane, typically operates at ambient pressure and temperature, and does not replicate flow-field-induced gradients or the mechanical compression experienced in practical PEMFC systems [29–34]. For these reasons, results obtained using the GDE half-cell should be regarded as semi-realistic. While they provide a substantially more representative assessment of CL behaviour than conventional rotating disk electrode (RDE) measurements, they do not fully capture the complexity of an operating PEMFC. Consequently, GDE experiments are best interpreted as complementary to single-cell testing, which remains indispensable for validating electrode performance under fully realistic operating conditions. Within this framework, the GDE half-cell constitutes an efficient and cost-effective screening platform, enabling rapid evaluation of electrode formulations with reduced material consumption and improved relevance to practical devices [29–34].

In this work, a multi-scale and methodologically structured experimental framework is developed to investigate how ionomer chemistry and I/C ratio govern CL architecture and, in turn, electrochemical performance. Nafion® is used as a benchmark, while Aquivion® D98 and D79® enable exploration of the interplay between proton conduction, catalyst accessibility, and interfacial structure. Central to this study is the use of a GDE half-cell platform as a controlled screening tool, where the direct contact between the CL and the liquid electrolyte ensures sufficient proton availability, effectively decoupling proton transport limitations from the intrinsic properties of the electrode. This enables a direct correlation between ink formulation parameters (i.e., ionomer chemistry and I/C ratio) and the resulting CL structure, allowing systematic identification of performance trends based on quantitative electrochemical descriptors.

The half-cell analysis is complemented by a comprehensive set of ex-situ characterization techniques, (FESEM, N_2 physisorption, XPS, and AFM–IR) to relate electrochemical behavior to morphology, porosity, and ionomer distribution. This integrated approach enables mechanistic interpretation of the electrochemical response in terms of underlying structural and interfacial features.

Finally, the optimized formulations identified through half-cell screening are validated in single-cell operation under realistic PEMFC conditions, where full transport phenomena are reintroduced. This combined workflow not only establishes a direct link between ionomer formulation, catalyst layer structure, and performance, but also critically assesses the extent to which half-cell observations can be translated to practical device operation.

Overall, this work demonstrates a reproducible and scalable experimental strategy for catalyst layer design, providing both mechanistic insight and a practical methodology for accelerated screening and optimization of PEMFC electrodes.

2. Methodology

2.1. Materials

In this study, three PFSA ionomers were investigated: a LSC ionomer, Nafion® (Sigma-Aldrich), used as benchmark, and two SSC ionomers, Aquivion® D98-25BS and Aquivion® D79-25BS (Sigma-Aldrich), hereafter referred to as Aquivion® D98 and Aquivion® D79, respectively.

Nafion® dispersion consists of an aqueous dispersion with an average solid content of 10 wt% (EW of 1100 g mol^{-1}, IEC of ~ 0.92 m_{eq} g^{-1}). Aquivion® dispersions contains 25 wt% solids. Aquivion® D98 exhibits an EW of 980 g mol^{-1} and an IEC of 1.02 m_{eq} g^{-1}, values broadly comparable to Nafion®. Aquivion® D79 features a markedly lower EW of 790 g mol^{-1}, corresponding to a higher IEC of approximately 1.27 m_{eq} g^{-1}.

CLs were prepared with a commercial benchmark catalyst, namely TEC10V50E manufactured by Tanaka Kikinzoku Kogyo, hereafter referred to as Pt/Vulcan. This material consists of platinum nanoparticles dispersed on a carbonaceous Vulcan XC72 support, with a nominal Pt loading of approximately 47 wt%.

Freudenberg H14C9 was used as GDL, consisting of a carbon paper substrate with a ~ 30 μm microporous layer (MPL) and a hydrophobic PTFE treatment, with a total thickness of ~ 180 μm under 1 MPa compression.

For MEA preparation, the commercial Nafion® 212 membrane was used, with a thickness of 50 μm.

2.2. Electrode preparation and MEA assembly

Catalyst inks were prepared by dispersing the catalyst and ionomer in a water-isopropanol solvent mixture, with a 1:1 water-to-isopropanol mass ratio. Solvent proportions were adjusted to maintain a solid content of 1 wt%. The I/C ratio was fixed at different values based on the experimental campaign.

To ensure homogeneity, the ink was magnetically stirred for 60 min at ambient temperature and subsequently sonicated in a water bath for 30 min under controlled temperature.

The ink was directly sprayed onto the MPL of the GDL, thereby producing a gas diffusion electrode (GDE). During deposition, the GDL was pre-heated and maintained at ~ 80 °C to promote rapid solvent evaporation.

The use of GDE method was motivated by the progressive and structured design of the experimental campaign. The study began with a systematic analysis of catalyst–ionomer interactions, carried out within a GDE half-cell setup, where the CL was tested without a membrane,

requiring direct deposition of the catalyst ink onto the MPL of the GDL. To enable a direct comparison between half-cell and single-cell results and to avoid introducing additional fabrication-related variables, the same deposition technique was therefore adopted for MEA preparation.

The platinum loading was fixed at 0.20 mg_{Pt} cm^{-2}, consistent with DOE targets for heavy-duty applications [35]. The actual loading was verified gravimetrically by weighing the GDL before and after deposition.

The resulting GDEs were cut to achieve the required dimensions depending on the final application.

For half-cell studies, electrodes with an active area of 5 × 3 cm^2 were prepared and tested directly in the setup.

For single-cell MEA assemblies, the electrodes were cut with an active area of 10 cm^2 to match the active area of the cell hardware.

MEAs for single-cell testing were prepared using the GDE method, as described above, ensuring consistency with the half-cell setup. For MEA fabrication, the membrane was hot pressed between two GDEs and two 140 μm-thick gaskets at 130 °C under 15 bar for 90 s. After hot pressing, the MEA was cooled under pressure to prevent mechanical stress.

2.3. Electrochemical testing protocol: configurations and procedures

2.3.1. GDE half-cell setup

The FlexCell-PTFE electrochemical test cell from Gaskatel was used for GDE half-cell measurements. The setup comprises a counter electrode compartment with liquid electrolyte and a Pt–Ir spiral counter electrode, a reversible hydrogen electrode (RHE, Mini-Hydroflex, Gaskatel) as reference, and a gas supply compartment. The liquid electrolyte is saturated continuosly with nitrogen to remove dissolved oxygen and avoid catalyst contamination.

The GDE served as working electrode, positioned at the interface between liquid electrolyte and gas phase. The CL faced the electrolyte, while the GDL side was exposed to a controlled flow of O_2 or N_2 through the gas compartment. The GDE was sealed with gaskets to prevent leakage, and electrical contact was provided by gold-plated plugs via the flow field. The cell configuration is schematically shown in Fig. S1 in the Supporting Information.

Electrochemical characterization in the GDE half-cell was performed with an Autolab potentiostat PGSTAT204 equipped with a Booster10A module. For impedance measurements, PalmSens potentiostat EmStat4S was used. All tests were conducted at ambient temperature and pressure, with 1 M $HClO_4$ as the liquid electrolyte. The gas feeds (O_2 or N_2) were humidified by passage through a fritted water bubbler, ensuring saturation at room temperature.

The electrolyte compartment was always filled with ultrapure water (Milli-Q, Merck) when not in use. Between tests and after each measurement campaign, the entire cell was thoroughly cleaned by boiling three times in ultrapure water to prevent contamination and ensure reproducibility.

A conditioning procedure was conducted prior to electrochemical testing to ensure catalyst surface cleanliness and stability. This consisted of cyclic voltammetry (CV) performed under humidified N_2 (300 mL min^{-1}) between + 0.05 V and + 1.2 V vs. RHE at a scan rate of 500 mV s^{-1} for 200 cycles. This was followed by a 5 min potential hold at 0.1 V vs. RHE under humidified O_2 supplied at 300 mL min^{-1}. The electrolyte was then replaced with fresh 1 M $HClO_4$ and the activation cycle was repeated to ensure a clean and reproducible electrode surface.

The ECSA was determined by CV under humidified N_2 at a flow rate of 300 mL min^{-1} between + 0.05 V to + 1.2 V vs. RHE at a scan rate of 100 mV s^{-1} for 10 cycles. The tenth cycle was used for evaluation. The ECSA was calculated by integrating the charge associated with hydrogen underpotential deposition (H_{upd}) after subtraction of the double-layer contribution.

Polarization measurements were conducted under humidified O_2 at 200 mL min^{-1} using a potentiostatic staircase protocol. The potential was swept from 1.05 to 0.1 V vs. RHE and back-forward, with a step size of 10 mV and a holding time of 10 s at each step. Three consecutive curves were recorded, and their average was taken as the representative response. All reported potentials were corrected for uncompensated resistance (R_0) determined from EIS.

EIS experiments were carried out under humidified O_2 at a flow rate of 200 mL min^{-1} at fixed potentials of 0.9 V and 0.8 V vs. RHE. Measurements were performed in potentiostatic mode with 5 mV AC perturbation, sweeping the frequency from 10,000 Hz to 0.1 Hz with 9.7 points per decade. Nyquist plots were used to analyse charge transfer and mass transport within the CL, while also enabling accurate determination of the R_0, used to correct all electrochemical data. Each measurement was repeated twice.

All electrochemical measurements were performed in triplicate on three independently prepared samples to ensure reproducibility and statistical reliability.

2.3.2. Single-cell setup

A commercial cell hardware supplied by Fuel Cell Technologies was used for MEA investigation. The cell consisted of two graphite end plates featuring a triple serpentine flow field design, with a nominal active area of 25 cm^2. The cell was connected to a Fuel Cell Technologies test station, which allows accurate control of temperature, pressure, and gas humidification. MEAs with an active area of 10 cm^2 were employed, by sealing the remaining area with gaskets to prevent crossover and ensure proper confinement of the reactive gases. The cell was assembled with a torque of 10 N m, applying gaskets on both the anode and cathode sides to achieve approximately 20% MEA compression.

Experiments were performed using a Biologic VSP-300 potentiostat equipped with a 20 A booster channel.

The break-in procedure was conducted under H_2 at 450 mL min^{-1} on the anode and air at 1100 mL min^{-1} on the cathode, both humidified to 100% RH at 80 °C and ambient pressure. The protocol consisted of 10 cycles, each combining a hold at 0.55 V vs. RHE for 45 min, an open circuit voltage (OCV) hold for 30 s, and a hold at 0.85 V for 10 min, followed by a recovery at 0.3 V vs. RHE for 5 h.

CV was performed at 80 °C and ambient pressure, with 100 mL min^{-1} H_2 at anode and 100 mL min^{-1} N_2 at cathode, both humidified to 100% RH. Five cycles were recorded between 0.1 and 1.0 V at 100 mV s^{-1}, and the average response was used for analysis.

Polarization measurements were conducted at 80 °C and ambient pressure. The anode was supplied with 650 mL min^{-1} H_2 and the cathode with 1300 mL min^{-1} air, both humidified to 100% RH. Three polarization curves were recorded by linear sweep voltammetry (LSV) between OCV and 0.1 V in forward and reverse mode at a scan rate of 10 mV s^{-1}. The average of the three curves was taken as representative. Additional polarization curves were recorded at ambient pressure, with the anode supplied with 650 mL min^{-1} H_2 and the cathode with 850 mL min^{-1} O_2, both humidified to 100% RH. Under these conditions, the potential was swept from OCV to 0.7 V and back at a scan rate of 10 mV s^{-1}.

EIS was performed at 80 °C and ambient pressure with 650 mL min^{-1} H_2 at anode and 1300 mL min^{-1} air at cathode, both humidified to 100% RH. Nyquist plots were recorded at 0.8 V with a 5 mV perturbation over the frequency range from 10,000 Hz to 0.1 Hz. Additional measurements were conducted under the same temperature, humidity, and pressure conditions, using 1000 mL min^{-1} H_2 at the anode and 2000 mL min^{-1} N_2 at the cathode, recorded at 0.4 V with the same perturbation amplitude and frequency range.

Hydrogen crossover was measured at 80 °C and ambient pressure with H_2 supplied to the anode at 1000 mL min^{-1} and N_2 to the cathode at 2000 mL min^{-1}, both humidified to 100% RH. LSV was performed between 0.1 and 0.5 V at 1 mV s^{-1}. Each measurement was repeated twice.

All electrochemical measurements were performed in triplicate on three independently prepared samples to ensure reproducibility and statistical reliability.

2.4. Ex-situ characterization

2.4.1. Field emission scanning electron microscopy (FESEM)

Top-view and cross-sectional images of the CLs deposited on GDLs were acquired using FESEM (Zeiss Merlin) equipped with a Gemini-II column and an Oxford x-act X-ray detector. Imaging was performed at an accelerating voltage of 3 kV in secondary electron (SE) mode and at 15 kV in backscattered electron (BSE) mode. Both top-view and cross-sectional imaging were performed to capture, as comprehensively as possible, the structural and morphological features of the CLs in both GDEs and MEAs investigated in this work.

Top-view images were collected directly on the CL surface in SE mode, providing detailed information on surface morphology and microstructure, particularly with respect to particle agglomeration and porosity. The same analysis was also used to evaluate crack formation, with crack density quantified from six independent top-view SEM micrographs collected at 150X magnification. Cross-sectional images were acquired in BSE mode to allow a clearer distinction of the CL from the adjacent PEM and GDL layers, since areas containing heavier elements (e.g., Pt) appear brighter compared to polymeric or carbon-based regions. The cross-sectional images were used to precisely evaluate CL thickness in both GDEs and MEAs. For this purpose, samples were immersed in liquid nitrogen and subsequently fractured to expose the cross-section. For each CL, 200 independent measurements were performed, and the thickness was determined by averaging these values to ensure statistical robustness and to account for possible inhomogeneities.

2.4.2. Nitrogen physisorption and BET analysis

N_2 physisorption experiments were carried out at 77 K using a Micromeritics ASAP 2020 analyser. The objective of the analysis was to characterize both the pristine catalyst and the corresponding CLs prepared with different ionomers, in order to evaluate the influence of the ionomer on surface area and porosity—particularly of the carbon support. This approach provides insight into how different ionomers interact with and distribute over the catalyst support surface depending on the specific catalyst–ionomer combination.

All catalysts and CLs were analyzed in powder form, with sample masses of approximately 90 mg. Prior to adsorption experiments, pristine catalysts were degassed at 150 °C for 2 h, while catalytic inks—prepared following the same procedure used for electrochemical tests—were dried overnight at 60 °C, loaded into the sample holder, and then degassed at 115 °C for 3 h. Adsorption measurements were performed immediately after degassing.

Adsorption isotherms for both catalysts and CLs were normalized to the carbon content of each sample. The Brunauer–Emmett–Teller (BET) method was applied in the relative pressure range of 0.05–0.3P/P_0 to determine the specific surface area (BET SA_{total}). The total pore volume ($V_{pore,total}$) was estimated at 0.98P/P_0 under standard conditions and converted using a factor of 0.001547, assuming that the density of condensed N_2 within the pores corresponds to that of bulk liquid N_2 [36].

Pore-size distributions were derived from the desorption branch of the isotherms using the Barrett–Joyner–Halenda (BJH) method [36,37]. The t-plot method was employed to determine the micropore volume ($V_{pore,<2\ nm}$) as well as the external and mesopore surface area ($SA_{>2\ nm}$). The thickness of the adsorbed layer on the pore wall t (Å) was calculated as a function of P/P_0 using the Harkins–Jura equation [36,37], and the isotherms were replotted as function of t:

$$t = \left(\frac{13.99}{0.034 - log\left(\frac{P}{P_0}\right)} \right)^{\frac{1}{2}} \quad (1)$$

The linear region of the isotherms between 5 and 15 Å was interpolated, with $SA_{>2}$ nm and $V_{pore,<2\ nm}$ obtained from the slope and intercept, respectively.

2.4.3. X-ray photoelectron spectroscopy

X-ray photoelectron spectroscopy (XPS) measurements were performed on Pt/Vulcan as-received catalyst powders, as well as on CLs containing both catalyst and ionomer, in order to assess surface composition, platinum electronic state, ionomer coverage, and metal–ionomer interactions. CL samples were prepared by cutting small pieces of sprayed electrodes and analyzed as intact layers. The surface composition of the different samples was investigated by XPS using a PHI 5000 VersaProbe instrument. Survey spectra were acquired with a pass energy of 187.85 eV, a take-off angle of 45°, and an X-ray spot diameter of 100 μm, while high-resolution (HR) spectra of C 1 s and Pt 4f were collected using a pass energy of 23.50 eV. All spectra were referenced to the C 1 s core level at 284.5 eV [36,38] to compensate for surface charging effects. Data analysis was performed using CasaXPS software.

2.4.4. Atomic force microscopy–infrared spectroscopy

Atomic force microscopy–infrared spectroscopy (AFM-IR) was employed to investigate the spatial distribution of ionomer phases on the surface of GDEs prepared with different ionomers (Nafion®, Aquivion® D98 and Aquivion® D79). All measurements were performed under controlled environmental conditions to ensure reproducibility and minimize instrumental drift.

Prior to analysis, all samples were allowed to equilibrate within the AFM chamber for approximately 48 h. Measurements were conducted at room temperature and 47% RH. During measurements, environmental fluctuations were maintained within ± 2 °C and ± 3% RH to minimize thermal and hygroscopic drift effects.

AFM-IR experiments were carried out using an Anasys nanoIR3-s atomic force microscope in tapping mode configuration. Commercial gold-coated silicon probes (Bruker PREX-TnIR-A) were used in all measurements, with a nominal spring constant of ~ 3N/m. The probes exhibited a fundamental resonance frequency in the range of 55–58 kHz. Scan rates were consistently maintained below 3 μm/s to ensure high spatial resolution and minimize tip–sample interaction artifacts.

A Daylight MIRcat-QT multichip quantum cascade laser (QCL) served as the infrared excitation source. The QCL pulse rate was tuned to the appropriate difference between the fundamental resonance frequency of the cantilever and one of its higher harmonics to allow for heterodyne detection of the IR signal amplitude.

All measurements followed the same experimental workflow, where laser power and duty cycle were optimized for each electrode system to maximize signal-to-noise ratio while avoiding local thermal effects and sample damage. For Nafion®-based samples, the laser was operated with ~ 60% of the average QCL laser power (0.5 W), a duty cycle of 10% and a pulse repetition rate of 998 kHz. For Aquivion®-based samples, ~15% of the average laser power, a duty cycle of 15% and a pulse rate of 945 kHz were used.

All AFM-IR images were processed and analyzed using Gwyddion software [39] as discussed below. Ionomer clusters smaller than 5 px after segmentation were discarded from the analysis to avoid artifacts arising from experimental noise.

3. Results and discussion

3.1. Optimization of the ionomer-to-carbon ratio in half-cell setup

The first stage of this study focused on optimizing the I/C ratio for Aquivion® D79 and Aquivion® D98, followed by benchmarking against Nafion®-based CLs. A GDE half-cell configuration was employed as a controlled and reliable screening platform, where direct electrolyte contact with the CL ensures efficient proton conduction and minimizes transport limitations. All materials, catalyst loadings, and fabrication

parameters were kept constant, with I/C ratio as the only variable.

For Aquivion®-based CLs, three I/C ratios (0.4, 0.6, and 0.8) were systematically investigated to capture the trade-off between proton conductivity, oxygen transport, and catalyst utilization. Nafion®-based electrodes were evaluated at I/C ratios of 0.6 and 0.8, selected as representative conditions for Pt/Vulcan systems commonly reported in the literature [3,40].

The optimal I/C ratio was identified through a comprehensive in-situ electrochemical assessment, including ECSA, mass and specific catalytic activities, charge transfer resistance (R_{ct}) and ohmic resistance (R_0). These descriptors were used to quantify the impact of ionomer content on the overall electrode performance and to define a consistent basis for comparisons with Nafion®-based systems.

Fig. S2 compares the CVs and the corresponding ECSA values of the Nafion®-based benchmark, Aquivion® D98 and Aquivion® D79 as a function of the I/C ratio. The observed trends directly reflect how ionomer chemistry governs catalyst accessibility through its impact on ionomer distribution and catalyst layer morphology.

For Aquivion® D98, ECSA increases monotonically with I/C ratio, highlighting the role of the ionomer in establishing progressive improvements in catalyst accessibility. In contrast, Aquivion® D79 exhibits non-linear behavior, with a clear optimum at intermediate ionomer content (I/C = 0.6). At low I/C ratio of 0.4, Aquivion D79 delivers higher ECSA compared to D98, evidencing its superior ability to establish proton-conducting pathways even under ionomer-lean conditions. This can be attributed to its SSC architecture and higher density of sulfonic acid groups, which promote the formation of thin, well-distributed ionomer nanofilms that preserve Pt accessibility [23,41]. At higher ionomer loading (I/C = 0.8), however, D79 shows a marked decline in ECSA, consistent with the formation of thicker and more compact ionomer domains that partially occlude Pt nanoparticles, thereby reducing catalyst accessibility [5].

For Nafion®-based GDEs, the ECSA values at 0.6 and 0.8 were nearly similar, confirming the negligible sensitivity of this ionomer to the I/C ratio in this range, as also reported by Lauf et al [40].

The observed differences among the ionomers and I/C ratios can be attributed to variations in ionomer–catalyst–solvent interactions, which govern the dispersion and organization of the ionomer within the catalyst layer. At fixed catalyst and solvent composition, the ionomer chemistry and loading determine its affinity for the carbon support and Pt surface, ultimately controlling ionomer film thickness, coverage, and spatial distribution [42]. In the GDE half-cell configuration, where the catalyst layer is in direct contact with the liquid electrolyte, proton transport limitations are effectively minimized. As a result, the measured electrochemical response is primarily governed by the structural properties of the catalyst layer, such as Pt accessibility and pore architecture, rather than by differences in intrinsic proton conductivity or ionomer network formation. Therefore, under these conditions, variations in ECSA and performance predominantly reflect changes in catalyst layer microstructure, driven by ionomer type and loading, affecting Pt exposure and the effective formation of the TPB.

To further rationalize these observations, Table 2 reports the Pt utilization efficiency, defined as the ratio between the experimentally measured ECSA and the theoretical surface area of the Pt nanoparticles. The latter was estimated by assuming spherical particles with an average diameter of 2.9 nm for the Pt/Vulcan catalyst previously calculated in ref. [43], and a Pt density of 21.4 g cm^{-3} [44]. The Pt utilization values indicate that an optimal I/C ratio and the use of the D79 ionomer lead to the highest Pt accessibility. Under GDE half-cell conditions, where the catalyst layer is in direct contact with the liquid electrolyte and proton transport limitations are strongly mitigated, the observed variations in Pt utilization are primarily governed by catalyst layer morphology and the effectiveness of TPB formation. This suggests that ionomer composition and content mainly act by tuning catalyst layer structure and Pt site exposure rather than by affecting ionic transport. This interpretation is further corroborated by ex-situ morphological analyses, which will be discussed in the following section.

Table 2
ECSA values and platinum utilization percentages for the different ionomer-based GDEs and I/C ratios.

Sample	I/C ratio	ECSA / $m^2\ g_{Pt}^{-1}$	Pt utilization / %
Nafion®	0.6	54.9	56.78
	0.8	53.9	55.75
Aquivion® D98	0.4	47.6	49.23
	0.6	53.2	55.03
	0.8	54.6	56.47
Aquivion® D79	0.4	51.3	53.06
	0.6	55.2	57.10
	0.8	49.6	51.30

The influence of the I/C ratio on electrode performance was further assessed through O_2 polarization measurements in the GDE half-cell configuration, enabling evaluation of how differences in catalyst accessibility and interfacial structure translate into effective electrochemical activity under operating conditions.

Fig. 1 (a, b) summarizes the iR-corrected polarization curves of Aquivion® D98- and D79-based electrodes at different I/C ratios.

The analysis was restricted to the kinetic and early ohmic region (OCV to ~ 0.8 V), as iR correction is particularly critical in GDE half-cells due to their higher uncompensated resistance (R_0) compared to single cells. The mass-transport regime was therefore excluded and is addressed in single-cell experiments discussed later in this work.

The polarization behaviour closely corroborated the trends previously observed in the ECSA measurements, with the best results recorded at I/C of 0.6, confirming the central role of ionomer content in governing catalyst utilization and reaction kinetics.

For comparison, Fig. S3 reports the polarization curves obtained for Nafion®-based GDEs at I/C of 0.6 and 0.8. The performance at the two ratios was nearly identical, with 0.6 showing slightly higher activity in the investigated potential range, in agreement with both the discussed ECSA data and the reported literature [3,40].

To quantify these trends, mass activity (I_m) and specific activity (J_S) values were extracted at 0.90 vs. RHE for all investigated systems, as reported in Fig. 1(c, d). Both metrics systematically peak at I/C of 0.6, regardless of the ionomer chemistry. Under GDE conditions, where proton transport limitations are minimized, this maximum reflects an optimal balance between Pt accessibility and interfacial morphology. The comparable activities obtained for Aquivion® D79, Aquivion® D98, and Nafion® at I/C = 0.6 further support this ratio as a robust benchmark for cross-ionomer comparison.

EIS was employed to further elucidate the resistive and interfacial contributions governing the observed performance trends. In particular, EIS provides direct insight into charge transport and reaction kinetics, allowing the roles of proton conduction, electronic resistance, and interfacial charge transfer to be quantitatively assessed. Measurements were therefore performed at 0.90 V vs. RHE and analysed using a Randles-type equivalent circuit, consisting of an inductive element (L) and an R_0 in series with a parallel RC element, comprising a constant phase element (CPE) representing the double-layer capacitance, and the R_{ct} associated with the cathodic oxygen reduction reaction (ORR) response of the GDE. Full spectra for all investigated MEAs and equivalent circuit scheme are provided in Fig. S4 and S5 of the Supporting Information, respectively.

The fitted parameters are summarized in Fig. 1 (e-f). Across all investigated systems, the uncompensated resistance R_0 was found to be approximately 4.5 Ω cm^2, consequently, the performance gaps can be reliably attributed to intrinsic electrode properties.

More pronounced differences emerged in the charge transfer resistance. For all ionomers, the lowest R_{ct} values were consistently observed at I/C = 0.6, in agreement with ECSA and polarization data. At this ratio, R_{ct} values converge to 9 – 9.5 Ω cm^2, indicating that, despite differences in chemical structure and acidity, a similar interfacial environment is

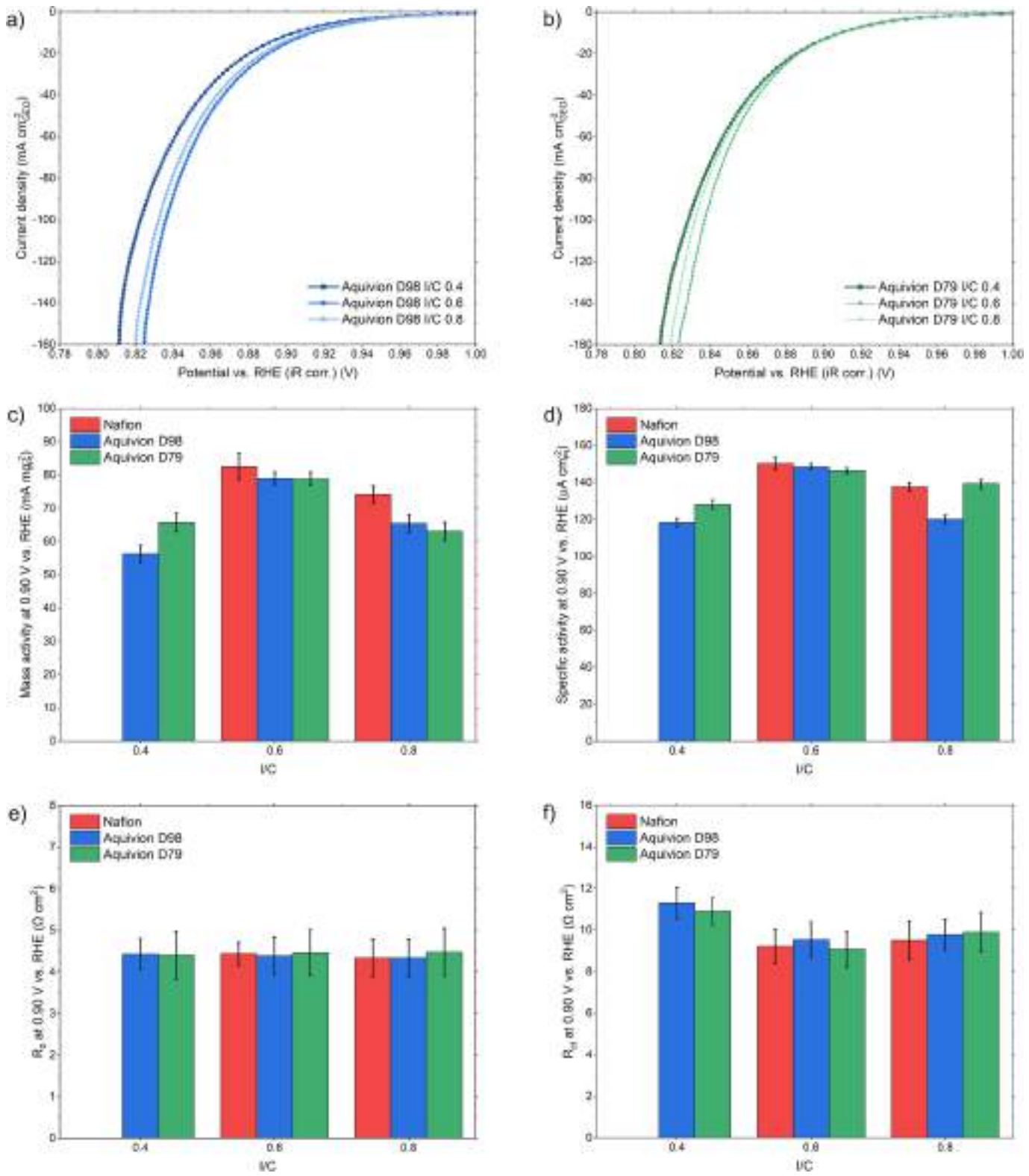

Fig. 1. (a, b) iR-corrected polarization curves of Aquivion® D98 and Aquivion® D79 GDEs, respectively, at different I/C ratios. (c) Mass activity (I_m) and (d) specific activity (J_S) of GDEs prepared with Nafion®, Aquivion® D98, and Aquivion® D79 at different I/C ratios, evaluated at 0.90 vs. RHE. (e) Ohmic resistance R_0 and (f) charge-transfer resistance R_{ct} of GDEs with Nafion®, Aquivion® D98, and Aquivion® D79 at different I/C ratios, obtained from fitting of Nyquist plots at 0.90 vs. RHE. Measurements were recorded under fully humidified O_2 conditions (200 mL min^{-1}) at ambient temperature and pressure.

established under optimized conditions.

Overall, the GDE half-cell configuration proved to be a highly effective platform for rapid optimization of the I/C ratio, allowing rapid and reproducible screening while reducing both material consumption and experimental time compared to conventional single-cell tests. The systematic analysis identified an I/C ratio of 0.6 as the optimal condition for all ionomers, reflecting an optimal balance between Pt accessibility and catalyst layer morphology. This convergence enables meaningful

comparison of ionomer chemistry at fixed composition, and subsequent analyses were therefore conducted at I/C = 0.6.

However, the half-cell configuration and the instrumentation employed restricted the analysis to the kinetic and part of the ohmic regions (OCV to ≈0.8 V), preventing reliable investigation of the mass-transport regime, where porosity and water management play a dominant role. For this reason, the evaluation of the high-current–density region was deferred to single-cell experiments, which are discussed in the following section.

3.2. Ex-situ morphological and structural characterization

Ex-situ characterization was performed on GDEs prepared at the optimized I/C ratio of 0.6 to directly assess how ionomer chemistry and EW influence the physical properties of the CL, including structure, porosity, surface characteristics and ionomer distribution. By isolating composition at fixed fabrication conditions, this analysis establishes a direct link between ionomer-dependent morphological features and the resulting electrochemical performance, providing a mechanistic explanation for the trends observed in the GDE screening.

Representative cross-section FESEM images (Fig. S6) confirm uniform adhesion at the CL–GDL interface and comparable CL thickness for all samples (Table S1), indicating that ionomer chemistry does not significantly influence macroscopic layer formation under the adopted conditions.

Low-magnification top-view FESEM images (Fig. 2 (a–c)) show similar surface roughness for all electrodes, with randomly distributed agglomerates typical of incomplete solvent evaporation during airbrush deposition [45], suggesting that large-scale morphology is primarily dictated by the fabrication method rather than ionomer type.

In contrast, clear ionomer-dependent effects emerge at smaller length scales. Fig. 2 (d–f) shows the systematic development of surface micro-cracks, with both crack density and length increasing as ionomer EW decreases.

The quantification of crack density, defined as the total crack length per unit surface area, confirms this trend (Table 3), indicating that low-EW ionomers promote mechanically less stable structures. This behavior is attributed to their higher hydrophilicity and the use of water-rich inks, which amplify capillary stresses during drying and lead to crack formation [4].

Table 3
Average crack density of CLs of GDEs prepared with Nafion®, Aquivion® D98, and Aquivion® D79 (I/C = 0.6). Crack density values were determined from six independent top-view SEM micrographs at 150X magnification.

Ionomer	Micro-crack density (mm^{-1})
Nafion®	1.77 ± 0.17
Aquivion® D98	1.93 ± 0.18
Aquivion® D79	2.34 ± 0.14

At higher magnification (Fig. 3), all CLs retain a highly porous structure; however, their internal organization differs markedly. Nafion®-based CLs display a more open macroporous morphology, whereas Aquivion®-based electrodes become progressively denser and more compact with decreasing EW. In particular, Aquivion® D79 CL exhibits particularly tight particle packing and a marked reduction in macropore volume, evidencing a transition toward a compact microstructure. These observations suggest that ionomer chemistry influences not only drying-induced stresses during film formation, but also ionomer–carbon interactions at the ink level, which govern particle rearrangement and pore stabilization [7].

Nitrogen physisorption measurements provide a quantitative basis for these morphological trends. As shown in Fig. 4(a), the pristine Pt/Vulcan catalyst exhibits a total surface area (SA_{total}) of 188.0 $m^2 g_{carbon}^{-1}$, with a micropore contribution ($SA_{<2nm}$) of 76.5 $m^2 g_{carbon}^{-1}$. Upon ionomer addition, both SA_{total} and $SA_{<2nm}$ decrease systematically with decreasing EW. Nafion® retains a relatively high SA_{total} of 169.6 $m^2 g_{carbon}^{-1}$, whereas Aquivion® D98 and D79 show progressively larger reductions to 148.3 $m^2 g_{carbon}^{-1}$, and 125.5 $m^2 g_{carbon}^{-1}$, respectively, indicating increasing pore filling.

A similar trend is observed for $SA_{<2nm}$, which is largely preserved in Nafion®-based CLs but significantly reduced in Aquivion® systems,

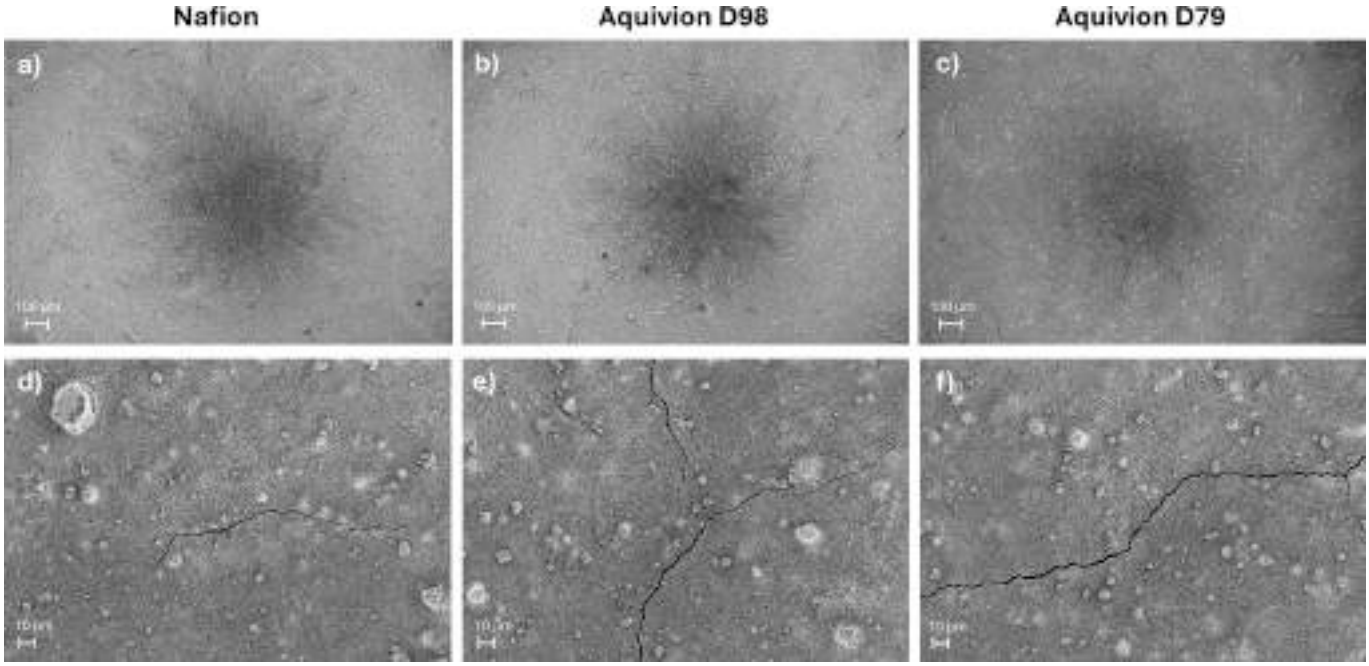

Fig. 2. Top-view FESEM SE images of CLs of GDEs prepared with Nafion®, Aquivion® D98, and Aquivion® D79 at I/C of 0.6. (a–c) Images at low magnification (150X) show surface roughness and the presence of agglomerates typical of airbrush-deposited electrodes. (d-f) Higher magnification images (1000X) highlight micro-cracks.

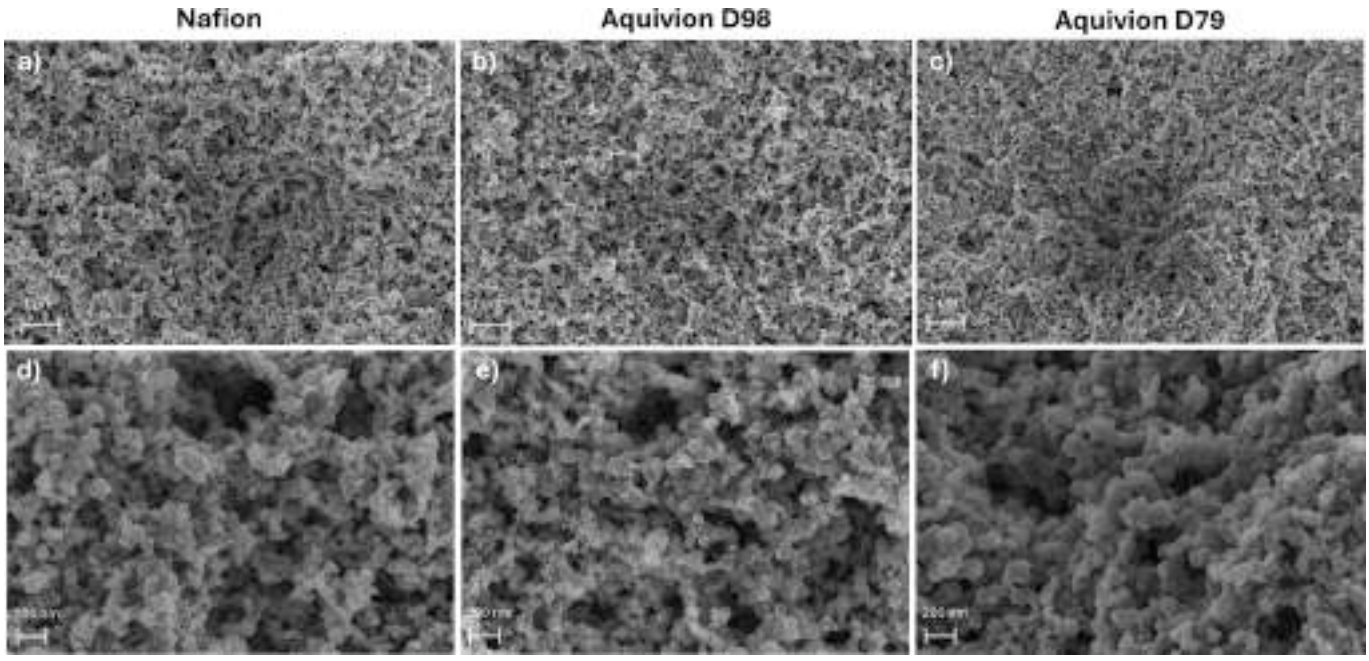

Fig. 3. High-magnification FESEM SE images of CLs of GDEs prepared with Nafion®, Aquivion® D98, and Aquivion® D79 at I/C of 0.6. (a–c) Images at 25′000X and (d–f) images at 100′000X allow evaluation of porosity.

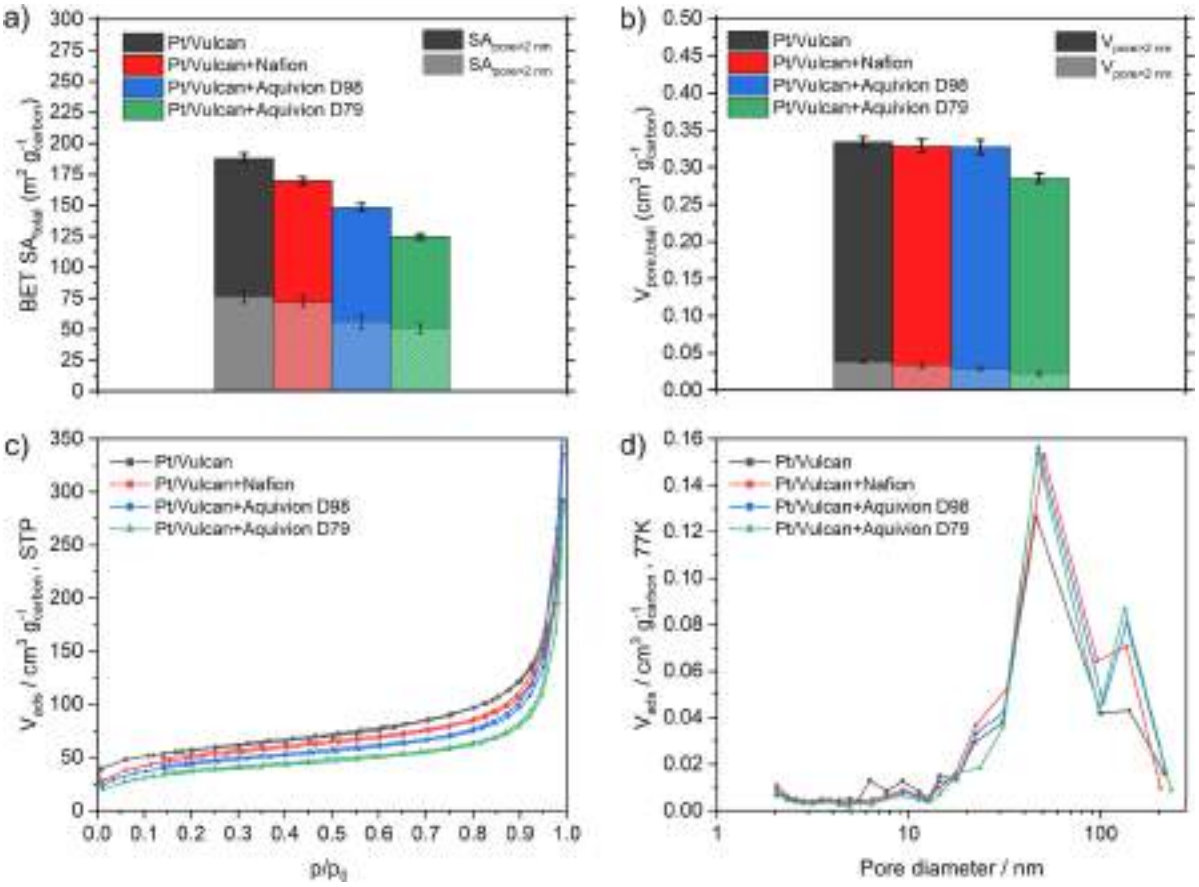

Fig. 4. Nitrogen physisorption analysis of pristine Pt/Vulcan catalyst and CLs prepared with Nafion®, Aquivion® D98, and Aquivion® D79 at an I/C ratio of 0.6. (a) Total BET surface area (SA_{total}), mesopore surface area ($SA_{>2nm}$), and micropore surface area ($SA_{<2nm}$). (b) Total pore volume ($V_{pore,total}$), mesopore volume ($V_{pore,>2nm}$), and micropore volume ($V_{pore,<2nm}$). (c) Nitrogen adsorption–desorption isotherms (d) and pore size distributions.

particularly for D79. This confirms that low-EW ionomers preferentially occupy micropores, thereby reducing accessible surface area. These findings are consistent with FESEM observations, showing that decreasing EW leads to denser structures and reduced pore accessibility of the CL. Given the importance of micropores for water management and oxygen transport at high current densities, this reduction has direct implications for mass-transport performance.

Pore volume data in Fig. 4(b) further supports these observations. While Nafion® and Aquivion® D98 induce only minor reductions in total pore volume, consistent with the formation of thin conformal ionomer films, Aquivion® D79 leads to a pronounced decrease, indicating substantial pore filling and structural densification.

The adsorption–desorption isotherms (Fig. 4(c)) are classified as type II according to IUPAC, reflecting the coexistence of micropores, which dominate the initial steep uptake, and macropores associated with large aggregates of carbon particles [37]. Importantly, ionomer incorporation shifts the isotherms downward without altering their overall shape, indicating that ionomers predominantly fill existing pores rather than modifying the carbon network morphology. Pore size distributions ((Fig. 4(d)) confirm that reductions are concentrated in the micro- and small mesopore range (<10 nm), with the strongest effect observed for Aquivion® D79, highlighting the trade-off between ionomer percolation and pore accessibility.

To further clarify the nature of this relationship and to gain insight into the interfacial interactions between ionomer, catalyst, and carbon support, XPS analyses were systematically performed on the pristine catalyst powder and on CL surfaces.

Survey spectra (Table S2) show a marked decrease in Pt 4f atomic concentration upon ionomer incorporation, consistent with partial masking of Pt nanoparticles. In parallel, the appearance of intense F 1 s signals, uniquely associated with the fluorinated backbone of PFSA, confirms successful ionomer coverage of the catalyst surface and provides direct spectroscopic evidence of its presence at the outermost surface within the typical XPS probing depth of approximately 5–10 nm.

High-resolution C 1 s spectra were deconvoluted as shown in Fig. S8 and Table S3. The fitting procedure included contributions from sp^2 C–C/C=C, sp^3 C–C, C–O/C=O, and O–C=O/COOH species, representative of the carbon support surface. Upon ionomer incorporation, two additional fluorinated components, namely C–F_2/O–CF_2 and C–F_3, were also considered to account for the PFSA backbone and side-chain moieties. Notably, the C–F_3 contribution is absent in Aquivion®-based ionomers, in agreement with their chemical structure. These fluorinated components provide further evidence of ionomer localization and distribution across the catalyst layer surface.

Table 4
Quantitative XPS analysis of the C 1 s and Pt 4f core-level spectra for pristine Pt/Vulcan catalyst and the corresponding catalyst layers after ionomer incorporation (Pt/Vulcan + Nafion®, Pt/Vulcan + Aquivion® D98, and Pt/Vulcan + Aquivion® D79). Values are reported as relative atomic concentrations (%conc) obtained from peak deconvolution, expressed in compact form and normalized to the total C 1 s or Pt 4f envelope.

	Pt/Vulcan	Pt/Vulcan + Nafion®	Pt/Vulcan + Aquivion® D98	Pt/Vulcan + Aquivion® D79
sp^2 C–C / C=C	49.1	42.4	40.1	42.6
sp^3 C–C	31.8	30.3	29.5	30.3
C–O / C=O	6.4	10.3	12.2	8.8
O–C=O / COOH	12.7	3.0	1.0	2.9
C–F_2 / O–CF_2	–	11.2	17.3	15.4
C–F_3	–	2.9	–	–
Pt^0	40.8	32.4	31.8	38.9
Pt^{2+}	31.0	35.4	36.0	31.2
Pt^{4+}	28.2	32.3	32.2	29.9

The results, summarized in Table 4, reveal that the relative contributions of sp^2 and sp^3 carbon remain comparable across all ionomers, indicating that differences in CL behavior are not driven by differential masking of amorphous and graphitic carbon domains. Variations in oxygen-containing species (C–O / C=O and O–C=O / COOH) mainly reflect the intrinsic chemical signature of the PFSA ionomers rather than major modifications of the carbon surface.

Similarly, the Pt 4f spectra were deconvoluted (Fig. S9 and Table S3), highlighting clear differences in ionomer–Pt interactions, as also summarized in Table 4. Nafion® and Aquivion® D98 show a similar reduction in metallic Pt^0 fraction and a corresponding increase in oxidized Pt species, consistent with strong sulfonic-acid–mediated interactions at the Pt surface. Aquivion® D79, however, retains a significantly higher Pt^0 fraction, indicating weaker and less intimate ionomer–Pt contact. It is worth noting that metallic Pt^0 is generally recognized as the electrochemically active state for catalytic reactions, whereas oxidized Pt species are typically associated with surface interactions involving oxygenated species or ionomer functional groups, such as sulfonic acid moieties.

These differences in Pt oxidation state and fluorine surface concentration suggest distinct interfacial chemistries among the investigated ionomers, which directly influence ORR kinetics. In particular, stronger ionomer–Pt interactions (as observed for Nafion® and Aquivion® D98) are expected to increase surface coverage by ionomer functional groups, potentially affecting oxygen adsorption/desorption equilibria at the Pt surface, whereas weaker interactions (as in Aquivion® D79) may preserve a higher fraction of metallic Pt sites, favoring intrinsic ORR activity.

These findings, together with the F 1 s and C 1 s analyses, provide a consistent picture of ionomer coverage and its interaction strength with Pt, although it should be noted that XPS does not provide direct spatial imaging but rather chemically resolved surface-sensitive information.

The spatial distribution of ionomer coverage over the three GDEs was directly assessed via AFM-IR [46–48]. This technique enables top-view mapping of the GDE surface, providing both qualitative visualization and semi-quantitative assessment of ionomer distribution at the nanoscale.

The highly porous structure of all three electrodes resulted in AFM topography maps (Fig. 5 (a-c)) displaying highly corrugated surface structures composed of individual grains ~ 60–70 nm in lateral size merging into larger (~200 nm) agglomerates. The values of mean square roughness (S_q) in Table 5 were comparable between the two Aquivion®-based GDE surfaces and ~ 1.6 times larger than that of the Nafion® GDE surface.

The corresponding AFM phase contrast maps (Fig. 5 (d-f)) provide qualitative insight into the ionomer distribution within the catalyst layer, as the phase signal is sensitive to local viscoelastic and adhesive properties. In this context, variations in phase contrast arise from differences in tip–sample interactions, where ionomer-covered regions (being more adhesive and dissipative) exhibit higher phase shifts, while exposed Pt/Vulcan areas (more elastic and less adhesive) show lower phase values [7,49,50].

The Nafion®-based GDE surface displays extended low-phase regions interspersed with large areas of nearly continuous high-phase signal, indicating a heterogeneous ionomer coverage with the formation of relatively large domains. In contrast, Aquivion®-based GDEs exhibit a more finely distributed phase contrast, characterized by smaller and more interconnected features. This behavior suggests a more homogeneous dispersion of Aquivion® within the catalyst layer, leading to a more uniform ionomer coverage at the microscale. Overall, the AFM analysis confirms that ionomer chemistry strongly influences not only nanoscale pore filling but also mesoscale surface organization, with direct implications for catalyst accessibility and TPB formation.

Finally, the corresponding AFM-IR chemical maps (Fig. 5 (g-i)) plot the normalized intensity of the IR absorption at 1060 cm^{-1}, corresponding to the IR absorption band of the symmetric stretching mode of

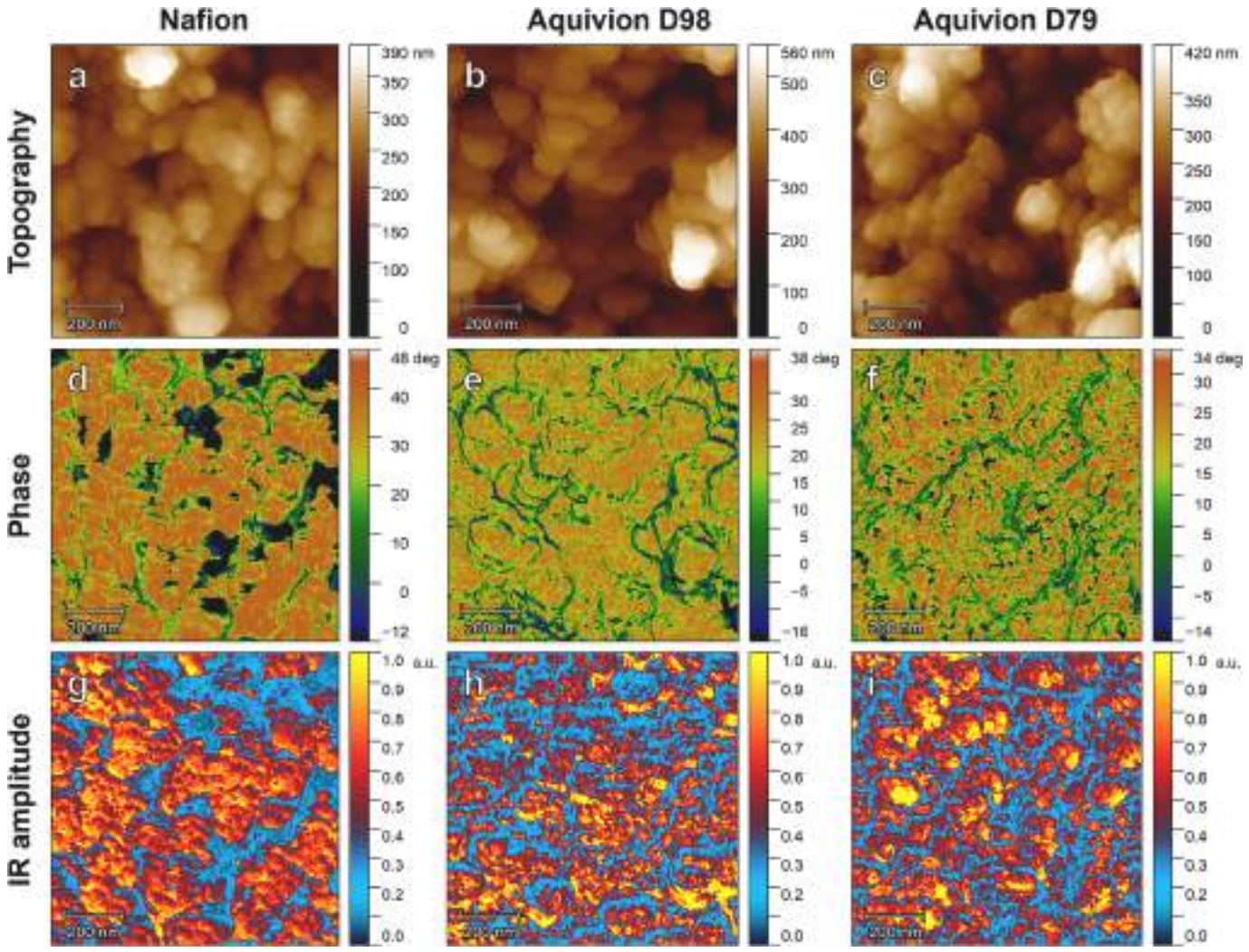

Fig. 5. AFM-IR images of CLs of GDEs prepared with Nafion®, Aquivion® D98, and Aquivion® D79 at I/C of 0.6. (a–c) Topography maps, (d–f) phase contrast maps, and (g-i) IR absorption amplitude maps at 1060 cm^{-1}.

Table 5
AFM-IR parameters of Pt/Vulcan GDEs after incorporation of different ionomers: mean-square roughness S_q, ionomer area coverage A_{im}, average ionomer domain size d_{im}, ionomer boundary length per unit area U_{im}, and Euler characteristic χ_E.

Ionomer	S_q (nm)	A_{im} (%)	d_{im} (nm)	U_{im} (μm^{-1})	χ_E (10^{-3})
Nafion®	44.66	52.6(1)	43(4)	47(1)	−3.65
Aquivion® D98	75.86	35.0(4)	27(3)	60(1)	8.06
Aquivion® D79	67.59	36.3(6)	27(3)	59(2)	11.22

the ionomer-specific SO_3^- functional group [51]. Qualitatively, the chemical maps confirm the morphology of ionomer coverage indirectly suggested by the phase images, with which they exhibit an excellent correlation. For a quantitative comparison of ionomer dispersion in the three GDEs, ionomer-covered areas were separated from the background by segmenting each image using Otsu's algorithm [52]. The following figures of merit of ionomer distribution were then computed for each GDE: the total area coverage (A_{im}), the average domain size (d_{im}), the boundary length of the domains per unit area (U_{im}), and the Euler characteristic (χ_E), which measures the connectivity of the domains [53–55].

As summarized in Table 5, the Nafion® GDE displays significantly larger A_{im} and d_{im} with respect to the Aquivion® GDEs, but a reduced U_{im}. Furthermore, the Nafion® coverage is characterized by a smaller, negative χ_E, Aquivion® D98 by a larger, positive χ_E, and Aquivion® D79 by the largest, positive χ_E. This indicates that, despite achieving a more extensive coverage of the GDE surface, Nafion® segregates into larger and more continuous domains, whereas Aquivion® D98 and D79 disperse into smaller, more evenly spread domains. Between the latter two, the higher χ_E value suggests that D79 may be achieving the better dispersion.

In conclusion, the observed structural differences can be consistently rationalized by ionomer–carbon interactions established at the ink stage, which govern CL formation and organization.

Nafion® is known to adsorb strongly onto Pt and carbon surfaces [7], as also indicated by the higher fraction of oxidized Pt species observed by XPS. This promotes preferential ionomer immobilization on catalyst particles and leads to the formation of relatively large ionomer domains within the ink. Upon drying, this results in a CL characterized by spatially extended but poorly interconnected ionomer regions, as confirmed by AFM–IR, together with a comparatively open porous structure observed by FESEM and N_2 physisorption.

Aquivion® D98 exhibits intermediate behavior, combining significant ionomer–catalyst interaction with a more homogeneous dispersion, leading to smaller and more interconnected ionomer domains while preserving pore accessibility.

In contrast, Aquivion® D79, due to its lower EW, shows weaker adsorption onto Pt/C surfaces [7], resulting in a higher fraction of free

ionomer in dispersion. This promotes the formation of a more continuous and finely distributed ionomer network, as confirmed by AFM–IR. At the same time, this enhanced connectivity leads to tighter particle packing and reduced pore volume, consistent with N_2 physisorption and FESEM observations.

Overall, these results indicate that ionomer chemistry governs a trade-off between ionomer network connectivity and pore accessibility, originating at the ink stage and determining CL architecture across multiple length scales. These structure–property relationships provide the basis for interpreting the electrochemical behavior observed in the GDE half-cell and will be further evaluated under realistic operating conditions in the following section.

3.3. Single-cell validation of optimized electrodes

Following the preliminary characterization in the GDE half-cell, single-cell PEMFC tests were performed to validate the electrochemical behavior of the electrodes and MEAs under realistic fuel cell operating conditions. First, H_2/O_2 polarization curves of MEA fabricated with Nafion®, Aquivion® D98, and Aquivion® D79 were recorded allowing direct comparison with half-cell measurements, as reported in Fig. 6.

Half-cell polarization curves were iR-corrected and acquired in O_2 under ambient pressure and temperature. Single-cell measurements were performed in O_2 at 80 °C, 100% RH, and ambient pressure, and were corrected for both ohmic resistance and hydrogen crossover. This consistent data treatment allows a reliable and artifact-free comparison between the two testing configurations.

The trends observed in half-cell measurements are preserved at the single-cell level, although some differences in performance arise when the same electrode system is tested in single-cell configuration due to the distinct operating conditions, particularly temperature and electrode–electrolyte configuration, including the absence of direct liquid electrolyte contact in the MEA.

Table 6 summarizes the electrochemical parameters obtained in single-cell configuration for the three MEAs: ECSA, H_2 crossover ($J_{crossover,H_2}$), mass activity (I_m), and specific activity (J_S) at 0.9 V, corrected for iR drop and H_2 crossover. These results reinforce the half-cell findings, demonstrating that the three ionomers perform equivalently in the kinetic and low-ohmic regions under realistic MEA operating conditions. Fig. S10 and Table S4 of the Supporting Information also provides CVs and the corresponding I_m and J_S at 0.8 V vs. RHE, respectively.

Table 6
Electrochemical surface area (ECSA), mass activity (I_m), and specific activity (J_S) at 0.9 V vs. RHE for MEAs fabricated with Nafion®, Aquivion® D98, and Aquivion® D79. Values are corrected for iR drop and H_2 crossover.

Ionomer	ECSA ($m^2\ g_{Pt}^{-1}$)	$J_{crossover,H_2}$ ($mA\ cm_{GEO}^{-2}$)	I_m at 0.90 V ($A\ g_{Pt}^{-1}$)	J_S at 0.90 V ($mA\ cm_{Pt}^{-2}$)
Nafion®	58.5 ± 1.7	0.38 ± 0.02	0.15 ± 0.01	0.26 ± 0.01
Aquivion® D98	56.9 ± 1.2	0.47 ± 0.03	0.15 ± 0.01	0.25 ± 0.01
Aquivion® D79	56.4 ± 1.3	0.60 ± 0.01	0.16 ± 0.01	0.27 ± 0.01

Switching from O_2 to air operation revealed subtle but systematic differences among the three ionomers, as detected in Fig. 7. While in the kinetic and intermediate voltage range (above ≈0.7 V) Nafion® and Aquivion®-based MEAs showed nearly identical performance, at higher current densities, where mass transport limitations become increasingly relevant, a clearer differentiation emerged. In this regime, Aquivion® D79 deviated more markedly, exhibiting consistently lower performance.

This behavior follows a clear EW-dependent trend and is fully consistent with the structural insights obtained from FESEM, BET, XPS and AFM-IR analyses. As demonstrated with AFM-IR mapping, the lower EW of Aquivion® D79 favors the formation of a more extended and percolated ionomer network, which enhances proton conduction. In parallel, this also leads to denser CL morphologies and reduced micro- and mesoporosity. As evidenced by nitrogen physisorption, Aquivion® D79 induces the largest loss in surface area and pore volume, particularly in the micropore range, while FESEM reveals a more compact particle packing. These features limit oxygen permeability and liquid water evacuation under air operation, amplifying mass-transport losses at high current density. By contrast, Aquivion® D98 combines weaker pore filling with more uniform ionomer coverage, resulting in transport properties closer to those of Nafion®, in agreement with their similar polarization behavior.

The polarization curves in Fig. 7 represent the average of three independent MEA measurements. Despite experimental variability, the

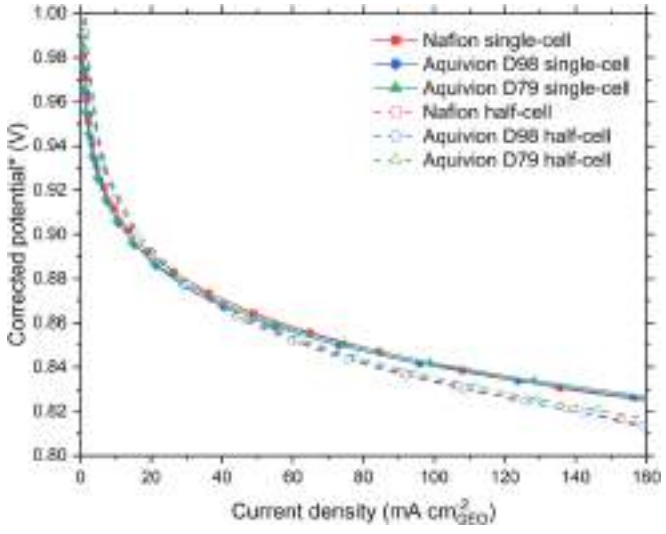

Fig. 6. Polarization curves of MEAs and GDE half-cells incorporating Nafion®, Aquivion® D98, and Aquivion® D79 ionomers. All electrodes were fabricated by the GDE method with an I/C ratio of 0.6, enabling a direct comparison between half-cell and single-cell configurations. Single-cell polarization curves were recorded at 80 °C, 100 % RH, and ambient pressure under O_2 and corrected for ohmic resistance and hydrogen crossover. GDE half-cell polarization curves were recorded under fully humidified O_2 flow (200 mL min^{-1}) at ambient temperature and pressure and were iR-corrected.

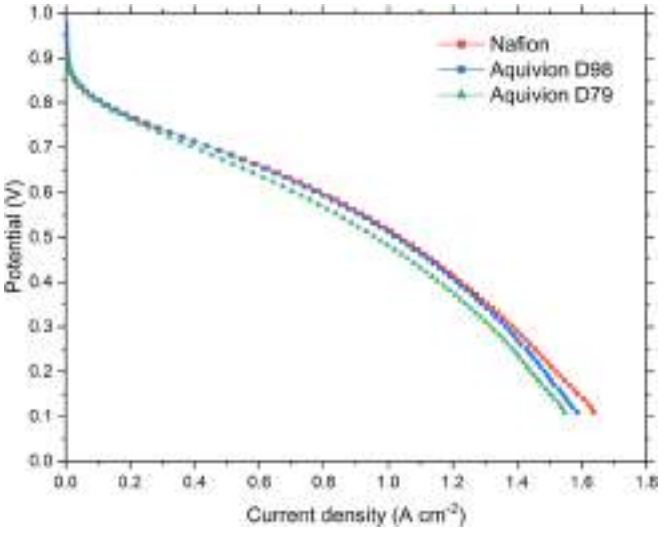

Fig. 7. Polarization curves in H_2/air (650/1300 mL min^{-1}) under 100% RH, 80 °C and ambient pressure for MEAs fabricated with Nafion®, Aquivion® D98, and Aquivion® D79 ionomers at I/C of 0.6.

performance hierarchy (Nafion® ≈ Aquivion® D98 > Aquivion® D79) is consistently reproduced, confirming that the observed differences are intrinsic and directly linked to ionomer-dependent CL organization rather than experimental scatter.

To further quantify these effects, Table 7 reports the current densities at 0.60, 0.40 V and 0.2 V, with the relative standard deviations.

EIS measurements were further carried out under H_2/air operation at 0.80 and 0.60 V. The Randles-type equivalent circuit used for data fitting and the Nyquist plots are reported in the Fig. S11 and S12 of the Supporting Information, respectively. Compared to the circuit employed for the half-cell analysis, the model was refined by including extra RC elements to account for the anodic contribution inherent to single-cell operation. The extracted parameters are summarized in Fig. 8 for all three MEAs at both investigated cell voltage.

The R_0 was found to be ≈100 $m\Omega\,cm^2$ for all MEAs—significantly lower than the ≈4.5 $\Omega\,cm^2$ observed in half-cell configuration, confirming the need for proper iR correction in GDE measurements. At 0.80 V, the cathode charge-transfer resistances ($R_{ct,c}$) were essentially identical across all ionomers, consistent with comparable activity in the kinetic region. At 0.60 V, however, differences emerged, reflecting the growing mass-transport penalties in Aquivion®-based MEAs at higher current densities.

Complementary EIS experiments in H_2/N_2 at 0.40 V were carried out to probe proton transport within the cathode CL to evaluate its dependence on ionomer type. The corresponding Nyquist plots are reported in the Fig. S13 of the Supporting Information. The spectra were accurately fitted using an equivalent circuit model which includes an L, an R_0, and a restricted linear diffusion element (M), as further represented in Fig. S14 of the Supporting Information.

The resulting protonic resistivities ($\rho_{H^+,cath}$) are summarized in Table 8. They were calculated by normalizing the proton resistance ($R_{H^+,cath}$) to the cathode CL thickness determined from FESEM cross-sectional analysis (Fig. S7 and Table S1 in the Supporting Information).

This systematic decrease in resistivity with decreasing EW reflects the intrinsic ionomer properties and their distribution within the CL. Low-EW SSC ionomers feature higher IEC, enhanced intrinsic proton conductivity, and weaker adsorption onto Pt/C surfaces, which collectively promote the formation of more continuous ionomer–catalyst networks. As evidenced by AFM-IR analysis, this results in a more homogeneous and better interconnected ionomer phase, facilitating efficient proton transport across the CL and ultimately leading to lower resistivity in Aquivion®-based electrodes compared to Nafion®.

To complement these electrochemical insights, ex-situ post-mortem analyses of MEA cross-sections were performed. Representative FESEM images are shown in Fig. S7 of the Supporting Information. All MEAs exhibited homogeneous layers regardless of ionomer type, confirming reproducible GDE-to-MEA transfer.

Comparison with pre-pressing values (Table S1) showed only minor thickness changes, indicating that hot pressing did not significantly compress or damage the CL microstructure. This finding is crucial, as optimal hot-pressing avoids excessive compression, which can induce membrane crossover, short circuits, porosity collapse, hinder oxygen/water transport, and reduce high-current–density performance, while insufficient compression leads to poor interfacial contact and increased ohmic resistance [56].

Table 7
Current densities at 0.60 V, 0.40 V and 0.2 V vs. RHE for MEAs fabricated with Nafion®, Aquivion® D98, and Aquivion® D79 ionomers at I/C of 0.6.

Ionomer	Current density at 0.6 V ($Ac\ m_{GEO}^{-2}$)	Current density at 0.4 V ($Ac\ m_{GEO}^{-2}$)	Current density at 0.2 V ($Ac\ m_{GEO}^{-2}$)
Nafion®	0.80 ± 0.04	1.23 ± 0.06	1.52 ± 0.07
Aquivion® D98	0.78 ± 0.04	1.21 ± 0.05	1.49 ± 0.09
Aquivion® D79	0.71 ± 0.05	1.16 ± 0.05	1.44 ± 0.08

Single-cell validation corroborates the trends identified in the GDE half-cell primarily within the kinetically controlled regime, confirming the reliability of the GDE-based approach for rapid screening of ionomer formulations and optimization of catalyst ink parameters, such as I/C ratio, when assessing intrinsic ORR activity and proton conduction. However, the limitations of the half-cell configuration become evident at higher current densities. The absence of a proton exchange membrane, operation at ambient pressure and temperature, and the lack of flow-field-induced gradients and mechanical compression prevent the GDE half-cell from fully reproducing the mass-transport phenomena characteristic of practical PEMFC operation.

In this regime, the impact of CL architecture becomes dominant, and clear differences among the ionomers emerge. In particular, the more open and accessible structures observed for Nafion® and Aquivion® D98 facilitate oxygen transport and liquid water removal, enabling stable performance at high current densities. In contrast, the denser microstructure associated with Aquivion® D79, resulting from its highly connected ionomer network, limits pore accessibility, leading to increased oxygen transport resistance and hindered water management. This results in the earlier onset of mass-transport limitations under air operation.

These findings demonstrate that, while ionomer chemistry can enhance proton conduction and catalyst accessibility at the nanoscale, optimal PEMFC performance requires a balanced CL architecture that simultaneously preserves pore connectivity and mass-transport pathways. Ultimately, the single-cell results confirm that the structural features established at the ink stage directly govern electrode performance under realistic operating conditions, highlighting the need for a holistic optimization of ink formulation to achieve the best trade-off between ionomer connectivity and pore accessibility.

4. Conclusions

The results of this study demonstrate that PEMFC CL performance is governed by the interplay between ionomer intrinsic properties, ionomer–catalyst interfacial interactions, and the resulting microstructure established already at the ink stage.

The combined use of GDE half-cell screening, ex situ characterization, and single-cell validation establishes a robust multi-scale framework to investigate these relationships. In particular, the GDE configuration enables rapid identification of optimal I/C ratios under conditions where proton transport limitations are minimized, allowing intrinsic catalyst accessibility and interfacial effects to be directly assessed. The trends identified at the half-cell level are consistently validated in single-cell operation, confirming the reliability of this approach while revealing the additional role of mass transport and water management under realistic PEMFC conditions.

Ex situ analyses (FESEM, N_2 physisorption, XPS, and AFM-IR) provide complementary insights into catalyst-layer organization across multiple length scales and clarify how ionomer chemistry governs structural evolution. In particular, Aquivion® D79 forms a more homogeneous and highly connected ionomer phase, which enhances proton conduction and lowers cathode protonic resistivity. However, this improved ionomer connectivity is accompanied by a denser CL morphology, leading to the earlier onset of mass-transport limitations under fully humidified single-cell operation. By contrast, Nafion® and Aquivion® D98 generate comparatively more open CL structures that preserve pore connectivity and facilitate gas transport and liquid–water removal, enabling stable performance at high current densities despite their lower intrinsic proton conductivity.

More broadly, this work underlines that maximizing ionomer proton conductivity alone does not ensure optimal electrode performance unless coupled with a CL architecture that preserves pore accessibility and efficient mass transport. Optimal performance therefore requires balancing ionomer connectivity with transport pathways, highlighting

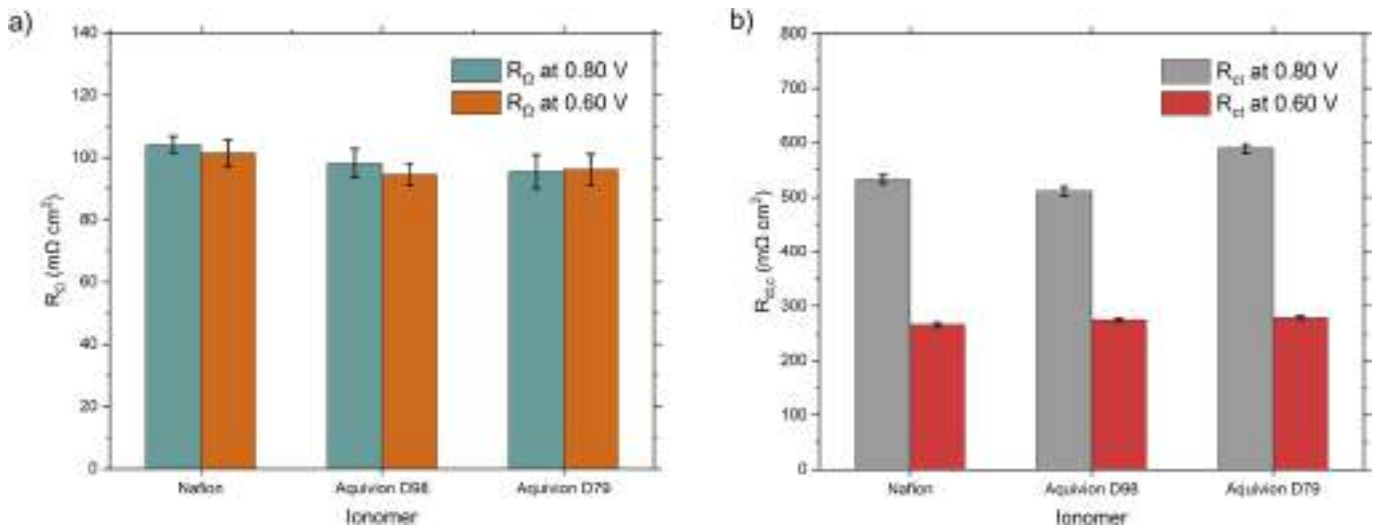

Fig. 8. Fitted values of (a) ohmic resistance (R_u) and (b) cathodic charge-transfer resistance ($R_{ct,c}$) extracted from the equivalent circuit analysis of EIS spectra at 0.80 and 0.60 V vs. RHE for MEAs with Nafion®, Aquivion® D98, and Aquivion® D79

Table 8
Proton resistivity of the cathode CL ($\rho_{H^+,cath}$) obtained from EIS measurements in H_2/N_2 at 0.40 V for MEAs prepared with Nafion®, Aquivion® D98, and Aquivion® D79. Values were calculated from fitted proton resistance normalized to CL thickness obtained from FESEM cross-section images and reported in table.

Ionomer	$\rho_{H^+,cath}$ at 0.40 V (Ω cm)	CL thickness in MEA (μm)
Nafion®	134.0 ± 0.83	4.72 ± 0.25
Aquivion® D98	78.9 ± 0.85	4.60 ± 0.29
Aquivion® D79	35.2 ± 0.94	4.51 ± 0.16

the critical role of ionomer adsorption, dispersion, and film formation during ink preparation.

While the present study specifically investigates the role of ionomer properties and ionomer–catalyst interactions, the results demonstrate how strongly these factors govern catalyst-layer microstructure and performance. Although the specific trends identified here are system-dependent, the multi-scale methodology combining GDE screening, ex situ characterization, and single-cell validation provides a robust and transferable framework for the optimization of a wide range of catalyst ink formulations. This approach enables systematic investigation of formulation–structure–performance relationships and can be readily extended to explore additional parameters in future studies, including alternative carbon supports, PFSA-free or hydrocarbon-based ionomers, advanced catalyst morphologies, different solvent systems, and catalyst-layer architectures designed for PEMFC electrodes.

CRediT authorship contribution statement

Giovanni Marco Carrabba: Writing – review & editing, Writing – original draft, Methodology, Investigation, Data curation. **Maria Chiara Massaro:** Writing – review & editing, Visualization, Methodology, Formal analysis, Data curation. **Erik Piatti:** Software, Methodology, Data curation. **Enrico Sartoretti:** Visualization, Methodology, Investigation. **Alessandro Hugo Antonio Monteverde:** Writing – review & editing, Supervision, Methodology, Funding acquisition, Conceptualization.

Declaration of competing interest

The authors declare that they have no known competing financial interests or personal relationships that could have appeared to influence the work reported in this paper.

Acknowledgments

The authors would like to express their sincere gratitude to Daniele Facchi and Lucia Mazzapioda from Syensqo for their invaluable support in conducting the tests and for their insightful discussions, and to Prof. Renato S. Gonnelli for fruitful scientific discussions concerning the scanning probe microscopy measurements. G. Carrabba acknowledges doctoral scholarship funding under the PNRR program (DM 352/22) through the "Next Generation EU" initiative of the European Union. In addition, the authors acknowledge the National Recovery and Resilience Plan (PNRR) and received funding from the Italian Ministry of the Environment and Energy Security, the "LightPEM" project, ID RSH2A_000033, CUP: F57G25000300006. E. Piatti also acknowledges funding by the European Union - Next Generation EU as part of the PRIN 2022 PNRR project "Continuous THERmal monitoring with wearable mid-InfraRed sensors'' (P2022AHXE5). The AFM-IR characterization was conducted at the facilities supported by the project "Dipartimento d'Eccellenza" of the Department of Applied Science and Technology at Politecnico di Torino.

Appendix A. Supplementary data

Supplementary data to this article can be found online at https://doi.org/10.1016/j.fuel.2026.140521.

Data availability

Data will be made available on request.

References

[1] Chen M, Zhao C, Sun F, Fan J, Li H, Wang H. Research progress of catalyst layer and interlayer interface structures in membrane electrode assembly (MEA) for

proton exchange membrane fuel cell (PEMFC) system. ETransportation 2020;5:100075. https://doi.org/10.1016/J.ETRAN.2020.100075.
[2] Wang Y, Ruiz Diaz DF, Chen KS, Wang Z, Adroher XC. Materials, technological status, and fundamentals of PEM fuel cells – a review. Mater Today 2020;32:178–203. https://doi.org/10.1016/J.MATTOD.2019.06.005.
[3] Qi Y, Morimoto Y, Shibata MS, Gao Z, Sabarirajan DC, Haug AT, et al. Understanding platinum ionomer interface properties of polymer electrolyte fuel cells. J Electrochem Soc 2022;169:064512. https://doi.org/10.1149/1945-7111/AC774F.
[4] Lei C, Bessarabov D, Ye S, Xie Z, Holdcroft S, Navessin T. Low equivalent weight short-side-chain perfluorosulfonic acid ionomers in fuel cell cathode catalyst layers. J Power Sources 2011;196:6168–76. https://doi.org/10.1016/j.jpowsour.2011.03.024.
[5] Gatto I, Saccà A, Sebastián D, Baglio V, Aricò AS, Oldani C, et al. Influence of ionomer content in the catalytic layer of MEAs based on Aquivion® ionomer. Polymers (Basel) 2021;13:3832. https://doi.org/10.3390/POLYM13213832.
[6] Wang H, Wang R, Sui S, Sun T, Yan Y, Du S. Cathode design for proton exchange membrane fuel cells in automotive applications. Automotive Innovation 2021;4:144–64. https://doi.org/10.1007/s42154-021-00148-y.
[7] Ren H, Teng Y, Meng X, Fang D, Huang H, Geng J, et al. Ionomer network of catalyst layers for proton exchange membrane fuel cell. J Power Sources 2021;506:230186. https://doi.org/10.1016/j.jpowsour.2021.230186.
[8] Suzuki T, Tsushima S, Hirai S. Effects of Nafion® ionomer and carbon particles on structure formation in a proton-exchange membrane fuel cell catalyst layer fabricated by the decal-transfer method. Int J Hydrogen Energy 2011;36:12361–9. https://doi.org/10.1016/j.ijhydene.2011.06.090.
[9] Delfino S, Villa DC, Giannetti A, Tomasino DV, Oldani C, Storti G, et al. Short Side-chain perfluorosulfonic acid aquivion: from production to application. Macromol Mater Eng 2025. https://doi.org/10.1002/mame.202500262.
[10] Kongkanand A, Mathias MF. The priority and challenge of high-power performance of low-platinum proton-exchange membrane fuel cells. J Phys Chem Lett 2016;7:1127–37. https://doi.org/10.1021/ACS.JPCLETT.6B00216/SUPPL_FILE/JZ6B00216_SI_001.PDF.
[11] Eskandari H, Paul DK, Young AP, Karan K. Humidity-dependent hydration and proton conductivity of PFSA ionomer thin films at fuel-cell-relevant temperatures: effect of ionomer equivalent weight and side-chain characteristics. ACS Appl Mater Interfaces 2022;14:50762–72. https://doi.org/10.1021/acsami.2c12667.
[12] Grimaldi A, Baricci A, De Antonellis S, Oldani C, Casalegno A. Experimental study and modeling of water transport through short-side-chain perfluorosulfonic acid membranes. J Power Sources 2023;558. https://doi.org/10.1016/j.jpowsour.2022.232556.
[13] Wang S, Song J, Zhao W, Guan P, Li M, Zhang M, et al. Nanostructures and multi-scale aggregation of high ion exchange capacity short-side-chain perfluorosulfonic acid dispersion. J Colloid Interface Sci 2024;672:805–13. https://doi.org/10.1016/j.jcis.2024.06.004.
[14] Cha D, Jeon SW, Yang W, Kim D, Kim Y. Comparative performance evaluation of self-humidifying PEMFCs with short-side-chain and long-side-chain membranes under various operating conditions. Energy 2018;150:320–8. https://doi.org/10.1016/j.energy.2018.02.133.
[15] Zhao N, Shi Z, Girard F. Superior proton exchange membrane fuel cell (Pemfc) performance using short-side-chain perfluorosulfonic acid (pfsa) membrane and ionomer. Materials 2022;15. https://doi.org/10.3390/ma15010078.
[16] Okada T, Xie G, Gorseth O, Kjelstrup S, Nakamura N, Arimura T. Ion and water transport characteristics of Nafion membranes as electrolytes. Electrochim Acta 1998;43:3741–7. https://doi.org/10.1016/S0013-4686(98)00132-7.
[17] Talukdar K, Gazdzicki P, Friedrich KA. Comparative investigation into the performance and durability of long and short side chain ionomers in Polymer Electrolyte Membrane fuel Cells. J Power Sources 2019;439:227078. https://doi.org/10.1016/J.JPOWSOUR.2019.227078.
[18] Li J, Singh JP, Neklyudov V, Stolov M, Yuan Z, Schilt Y, et al. Anisotropic membrane with high proton conductivity sustaining upon dehydration. Sci Adv 2024;10:eadp1450. https://doi.org/10.1126/SCIADV.ADP1450.
[19] Liu L, Chen W, Li Y. An overview of the proton conductivity of nafion membranes through a statistical analysis. J Memb Sci 2016;504:1–9. https://doi.org/10.1016/J.MEMSCI.2015.12.065.
[20] Li T, Shen J, Chen G, Guo S, Xie G. Performance comparison of proton exchange membrane fuel cells with nafion and aquivion perfluorosulfonic acids with different equivalent weights as the electrode binders. ACS Omega 2020;5:17628–36. https://doi.org/10.1021/acsomega.0c02110.
[21] Devrim Y, Albostan A. Enhancement of PEM fuel cell performance at higher temperatures and lower humidities by high performance membrane electrode assembly based on Nafion/zeolite membrane. Int J Hydrogen Energy 2015;40:15328–35. https://doi.org/10.1016/J.IJHYDENE.2015.02.078.
[22] Yan Q, Toghiani H, Causey H. Steady state and dynamic performance of proton exchange membrane fuel cells (PEMFCs) under various operating conditions and load changes. J Power Sources 2006;161:492–502. https://doi.org/10.1016/J.JPOWSOUR.2006.03.077.
[23] Garsany Y, Atkinson RW, Sassin MB, Hjelm RME, Gould BD, Swider-Lyons KE. Improving PEMFC performance using short-side-chain low-equivalent-weight PFSA ionomer in the cathode catalyst layer. J Electrochem Soc 2018;165:F381–91. https://doi.org/10.1149/2.1361805jes.
[24] Balogun EO, Hussain N, Chamier J, Barendse P. Performance and durability studies of perfluorosulfonic acid ionomers as binders in PEMFC catalyst layers using Electrochemical Impedance Spectroscopy. Int J Hydrogen Energy 2019;44:32219–30. https://doi.org/10.1016/J.IJHYDENE.2019.10.079.
[25] Shahgaldi S, Alaefour I, Li X. The impact of short side chain ionomer on polymer electrolyte membrane fuel cell performance and durability. Appl Energy 2018;217:295–302. https://doi.org/10.1016/j.apenergy.2018.02.154.
[26] Aquivion® E87-05S n.d. https://www.fuelcellstore.com/solvay-aquivion-e87-05s-72700000?utm_source=chatgpt.com (accessed September 14, 2025).
[27] Siracusano S, Oldani C, Navarra MA, Tonella S, Mazzapioda L, Briguglio N, et al. Chemically stabilised extruded and recast short side chain Aquivion® proton exchange membranes for high current density operation in water electrolysis. J Memb Sci 2019;578:136–48. https://doi.org/10.1016/J.MEMSCI.2019.02.021.
[28] Peron J, Edwards D, Haldane M, Luo X, Zhang Y, Holdcroft S, et al. Fuel cell catalyst layers containing short-side-chain perfluorosulfonic acid ionomers. J Power Sources 2011;196:179–81. https://doi.org/10.1016/J.JPOWSOUR.2010.06.050.
[29] Riasse R, Lafforgue C, Vandenberghe F, Micoud F, Morin A, Arenz M, et al. Benchmarking proton exchange membrane fuel cell cathode catalyst at high current density: a comparison between the rotating disk electrode, the gas diffusion electrode and differential cell. J Power Sources 2023;556. https://doi.org/10.1016/j.jpowsour.2022.232491.
[30] Schmitt N, Schmidt M, Mueller JE, Schmidt L, Trabold M, Jeschonek K, et al. Which insights can gas diffusion electrode half-cell experiments give into activity trends and transport phenomena of membrane electrode assemblies? Energy Adv 2023;2:854–63. https://doi.org/10.1039/d3ya00055a.
[31] Ehelebe K, Schmitt N, Sievers G, Jensen AW, Hrnjić A, Collantes Jiménez P, et al. Benchmarking fuel cell electrocatalysts using gas diffusion electrodes: inter-lab comparison and best practices. ACS Energy Lett 2022;7:816–26. https://doi.org/10.1021/acsenergylett.1c02659.
[32] Loukrakpam R, Gomes BF, Kottakkat T, Roth C. A bird's eye perspective of the measurement of oxygen reduction reaction in gas diffusion electrode half-cell set-ups for pt electrocatalysts in acidic media. JPhys Mater 2021;4. https://doi.org/10.1088/2515-7639/ac0319.
[33] Pinaud BA, Bonakdarpour A, Daniel L, Sharman J, Wilkinson DP. Key considerations for high current fuel cell catalyst testing in an electrochemical half-cell. J Electrochem Soc 2017;164:F321–2. https://doi.org/10.1149/2.0891704jes.
[34] Ehelebe K, Seeberger D, Paul MTY, Thiele S, Mayrhofer KJJ, Cherevko S. Evaluating electrocatalysts at relevant currents in a half-cell: the impact of Pt loading on oxygen reduction reaction. J Electrochem Soc 2019;166:F1259–68. https://doi.org/10.1149/2.0911915jes.
[35] Anl) (, Wang X. DOE Hydrogen Program Record 24004: Heavy-Duty Fuel Cell System Cost – 2023. 2023.
[36] Massaro MC, Carrabba GM, Sartoretti E, Ostroverkh A, Artusio F, Pisano R, et al. Synergistic enhancement of PEM fuel cell performance for heavy-duty applications: PtCo/N-doped carbon catalyst and short-side-chain ionomer integration. J Power Sources 2026. https://doi.org/10.1016/j.jpowsour.2026.239323.
[37] Soboleva T, Zhao X, Malek K, Xie Z, Navessin T, Holdcroft S. On the micro-, meso-, and macroporous structures of polymer electrolyte membrane fuel cell catalyst layers. ACS Appl Mater Interfaces 2010;2:375–84. https://doi.org/10.1021/am900600y.
[38] Patel A, Artyushkova K, Atanassov P, Colbow V, Dutta M, Harvey D, et al. Investigating the effects of proton exchange membrane fuel cell conditions on carbon supported platinum electrocatalyst composition and performance. J Vac Sci Technol A 2012;30. https://doi.org/10.1116/1.4707153.
[39] Nečas D, Klapetek P. Gwyddion: an open-source software for SPM data analysis. Cent Eur J Phys 2012;10:181–8. https://doi.org/10.2478/s11534-011-0096-2.
[40] Lauf P, Morales AL, Ehelebe K, Hutzler A, Mayrhofer KJJ, Lloret V, et al. Benchmarking performance and degradation of Pt supported on different carbons for PEMFC applications using gas diffusion electrode half-cell. ACS Appl Energy Mater 2025;8:7939–47. https://doi.org/10.1021/ACSAEM.5C00184.
[41] Shahgaldi S, Alaefour I, Zhao J, Li X. Impact of ionomer in the catalyst layers on proton exchange membrane fuel cell performance under different reactant flows and pressures. Fuel 2018;227:35–41. https://doi.org/10.1016/j.fuel.2018.04.076.
[42] Berlinger SA, Garg S, Weber AZ. Multicomponent, multiphase interactions in fuel-cell inks. Curr Opin Electrochem 2021;29. https://doi.org/10.1016/j.coelec.2021.100744.
[43] Carrabba GM, Sartoretti E, Parisi E, Simone E, Monteverde AHA. Carbon corrosion resistance in PEM fuel cells: Comparative study of short and long side chain perfluorosulfonic acid ionomers. Int J Hydrogen Energy 2025;133:546–59. https://doi.org/10.1016/j.ijhydene.2025.04.262.
[44] Cheng X, Yi B, Han M, Zhang J, Qiao Y, Yu J. Investigation of platinum utilization and morphology in catalyst layer of polymer electrolyte fuel cells. vol. 79. 1999.
[45] Talukdar K, Morawietz T, Sarkezi-Selsky P, Yezerska K, Sergeev O, Heger JF, et al. Exploring critical parameters of electrode fabrication in polymer electrolyte membrane fuel cells. J Power Sources 2022;540:231638. https://doi.org/10.1016/J.JPOWSOUR.2022.231638.
[46] Prater C, Kjoller K, Shetty R. Nanoscale infrared spectroscopy. vol. 13. 2010.
[47] Dazzi A, Prater CB. AFM-IR: Technology and applications in nanoscale infrared spectroscopy and chemical imaging. Chem Rev 2017;117:5146–73. https://doi.org/10.1021/acs.chemrev.6b00448.
[48] Piatti E, Montagna Bozzone J, Daghero D. Anomalous metallic phase in molybdenum disulphide induced via gate-driven organic ion intercalation. Nanomaterials 2022;12. https://doi.org/10.3390/nano12111842.
[49] Morawietz T, Handl M, Oldani C, Friedrich KA, Hiesgen R. Quantitative in situ analysis of ionomer structure in fuel cell catalytic layers. ACS Appl Mater Interfaces 2016;8:27044–54. https://doi.org/10.1021/acsami.6b07188.
[50] García R, Tamayo J, Calleja M, García F. Phase contrast in tapping-mode scanning force microscopy. vol. 66. 1998.

[51] Agarwal T, Prasad AK, Advani SG, Babu SK, Borup RL. Infrared spectroscopy for understanding the structure of Nafion and its associated properties. J Mater Chem A Mater 2024;12:14229–44. https://doi.org/10.1039/d3ta05653h.
[52] Otsu N. A threshold selection method from gray-level histograms. IEEE Trans Syst Man Cybern 1979:SMC-9. https://doi.org/10.1109/TSMC.1979.4310076.
[53] Wang J, Müller M. Microphase separation of mixed polymer brushes: dependence of the morphology on grafting density, composition, chain-length asymmetry, solvent quality, and selectivity. J Phys Chem B 2009;113:11384–402. https://doi.org/10.1021/jp903161j.
[54] Raczkowska J, Rysz J, Budkowski A, Lekki J, Lekka M, Bernasik A, et al. Surface patterns in solvent-cast polymer blend films analyzed with an integral-geometry approach. Macromolecules 2003;36:2419–27. https://doi.org/10.1021/ma020870w.
[55] Vasconcelos HC, Eleutério T, Meirelles M, Özmenteş R. When a surface becomes a network: SEM reveals hidden scaling laws and a percolation-like transition in thin films. Surfaces 2026;9. https://doi.org/10.3390/surfaces9010014.
[56] Paganin VA, Sakita AMP, Lopes T, Ticianelli EA, Perez J. Uncovering key parameters in perfluorosulfonic acid (PFSA) membrane fuel cells to enhance performance. Membranes (Basel) 2025;15:65. https://doi.org/10.3390/MEMBRANES15030065/S1.